Geological Evolution of Titan's Equatorial Regions: Possible Nature and Origin of the Dune Material

Jeremy Brossier, Sébastien Rodriguez, Thomas Cornet, Antoine Lucas, Jani Radebaugh, Luca Maltagliati, Stéphane Le Mouélic, Anezina Solomonidou, Athena Coustenis, Mathieu Hirtzig, et al.

Journal of Geophysical Research: Planets

RESEARCH ARTICLE
10.1029/2017JE005399

Geological Evolution of Titan's Equatorial Regions: Possible Nature and Origin of the Dune Material

J. F. Brossier[1], S. Rodriguez[2], T. Cornet[3,4], A. Lucas[2], J. Radebaugh[5], L. Maltagliati[6], S. Le Mouélic[7], A. Solomonidou[4,8], A. Coustenis[9], M. Hirtzig[10], R. Jaumann[1], K. Stephan[1], and C. Sotin[8]

[1]Institute of Planetary Research, German Aerospace Center (DLR), Berlin, Germany, [2]Institut de Physique du Globe de Paris, CNRS-UMR 7154, Université Paris-Diderot, USPC, Paris, France, [3]Laboratoire Astrophysique, Instrumentation et Modélisation, CNRS-UMR 7158, Université Paris-Diderot, USPC, CEA-Saclay, Gif-sur-Yvette, Paris, France, [4]European Space Agency, European Space Astronomy Center, Madrid, Spain, [5]Department of Geological Sciences, Brigham Young University, Provo, UT, USA, [6]Nature Publishing Group, London, UK, [7]Laboratoire de Planétologie et Géodynamique, CNRS-UMR 6112, Université de Nantes, Nantes, France, [8]Jet Propulsion Laboratory, California Institute of Technology, Pasadena, CA, USA, [9]Laboratoire d'études spatiales et d'instrumentation en astrophysique, Observatoire de Paris, CNRS, UPMC Université Paris 06, Université Paris-Diderot, Meudon, France, [10]Fondation "La main à la pâte", Montrouge, France

Abstract In 13 years, infrared observations from the Visual and Infrared Mapping Spectrometer onboard Cassini provided significant hints about the spectral and geological diversity of Titan's surface. The analysis of the infrared (IR) signature of spectral units enables constraining the surface composition, which is crucial for understanding possible interactions between Titan's interior, surface, and atmosphere. Here we investigate a selection of areas in the equatorial regions, imaged by Cassini's instruments, which exhibit an apparent transition from the Visual and Infrared Mapping Spectrometer IR-bright to the IR-blue and IR-brown units (from false-color composites using red: 1.57/1.27 μm, green: 2.01/1.27 μm, and blue: 1.27/1.08 μm). By applying an updated radiative transfer model, we extract the surface albedo of IR units identified in these regions. Then, we compare them with synthetic mixtures of two expected components on Titan's surface, namely, water ice and laboratory tholins. This allows us to reconnect the derived composition and grain size information to the geomorphology observed from Radio Detection and Ranging instrument (RADAR)/Synthetic Aperture Radar images. We interpret IR-bright units as hills and plains coated by organic material and incised by fluvial networks. Erosion products are transported downstream to areas where IR-blue units are seen near the IR-bright units. These units, enriched in water ice, are most likely outwash plains hosting debris from fluvial erosion. Farther away from the IR-bright units, the IR-brown units are dominantly made of organics with varied grain sizes, ranging from dust- to sand-sized particles that form the dune fields. The transition areas therefore exhibit trends in water ice content and grain size supported by geomorphological observations.

Key Points:
- Infrared properties and geological relationships of Titan's spectral units have been investigated in the equatorial regions
- New insights on the composition and granulometry of the infrared units are given by coupling radiative transfer and spectral mixing models
- The distribution of Titan's infrared units is similar to the transition from mountains to stony and sandy deserts on Earth

Supporting Information:
- Supporting Information S1

Correspondence to:
J. F. Brossier,
jeremy.brossier@dlr.de

Citation:
Brossier, J. F., Rodriguez, S., Cornet, T., Lucas, A., Radebaugh, J., Maltagliati, L., et al. (2018). Geological evolution of Titan's equatorial regions: Possible nature and origin of the dune material. *Journal of Geophysical Research: Planets*, *123*, 1089–1112. https://doi.org/10.1029/2017JE005399

Received 22 JUL 2017
Accepted 6 APR 2018
Accepted article online 17 APR 2018
Published online 7 MAY 2018

1. Introduction

Since 2004, the Visual and Infrared Mapping Spectrometer (VIMS) (Brown et al., 2004), onboard the Cassini spacecraft, has observed at full coverage the equatorial belt of Titan (±40° latitude). VIMS false-color composite images are produced by using a color scheme of simple channels (red: average over 4.90–5.12 μm, green: 2.01 μm, and blue: 1.27 μm in Figure 1a) or even ratios of channels (red: 1.57/1.27 μm, green: 2.01/1.27 μm, and blue: 1.27/1.08 μm) in the near-IR range. The analysis of the two types of composites enables the identification of four main spectral units at the lower latitudes (Barnes, Brown, et al., 2007; Soderblom et al., 2007): (1) the IR-bright, (2) the IR-brown, (3) the IR-blue, and (4) the 5-μm bright units. IR-bright units appear to correspond to mountainous terrains, craters (ejecta, rims, and central peak), and most plains (notably undifferentiated and variable plains as described in Lopes et al., 2010, 2016; Malaska, Lopes, Williams, et al., 2016) and are assumed to be formed by a layer of organic sediments similar to the atmospheric aerosols coating Titan's substratum. IR-brown units are strongly correlated with the dunes as seen by Cassini's RADAR (Rodriguez et al., 2014; Soderblom et al., 2007) and are most likely made of organic sand-like particles. IR-blue units are thought to be enriched in water ice with respect to the rest of Titan's surface and possibly result from icebed material excavated by impacts (Le Mouélic et al., 2008) and fluvial erosion upon this icebed (Barnes, Radebaugh, et al., 2007; Jaumann et al., 2008, 2010; Rodriguez et al., 2006). The last spectral unit is very bright at longer VIMS wavelengths and therefore named 5-μm bright units and is often interpreted as

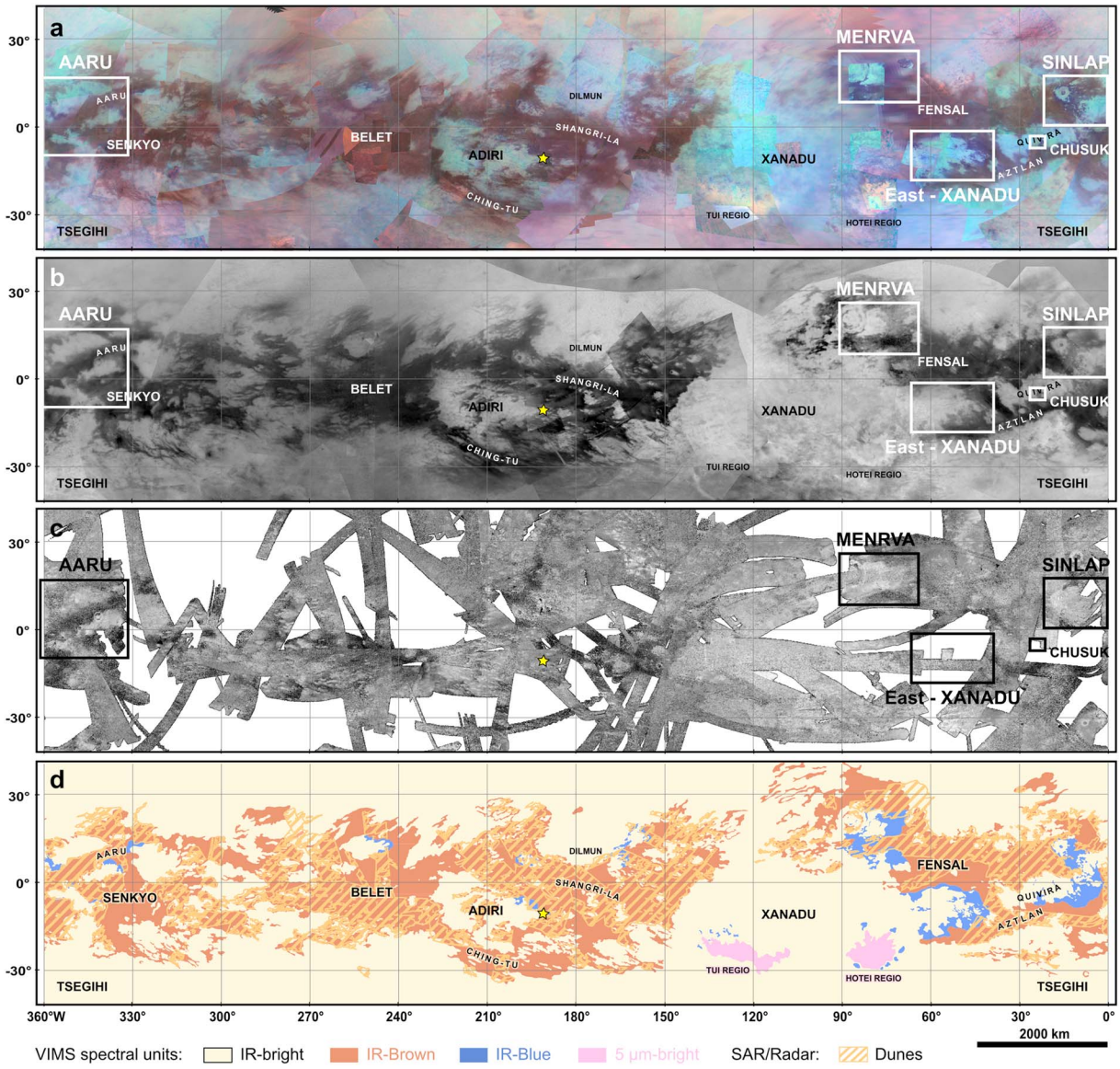

Figure 1. Equatorial maps of Titan within 40° of latitude. (a) False-color composite of simple VIMS channels (red: average over 4.90–5.12 μm, green: 2.01 μm, and blue: 1.27 μm) (Le Mouélic et al., 2016). (b) Near-IR Imaging Science Subsystem observations at 0.938 μm collected up to flyby T100 in April 2014 (NASA/JPL-Caltech/Space Science Institute, PIA19658). (c) Mosaic of SAR swaths at 2.18 cm through flyby T120 (June 2016) and covering about 65.7% of the total Titan's surface. (d) Color-coded map of the spectral units and the SAR dunes by using these combined data sets. The IR-brown units cover about 18.6% of the total Titan's surface, while the IR-blue units represent only 1.5%. These maps are displayed in a simple cylindrical projection centered at 180°W and 0°N, with names of prominent surface units. The frames in the first three maps indicate location of the regions selected for this study: Sinlap crater, Aaru Regio, Menrva crater, eastern Xanadu, and Chusuk Planitia (see Figures 2–5, respectively). The yellow star in all the maps indicates the location of the Huygens landing site (192.4°W, 10.2°S). VIMS = Visual and Infrared Mapping Spectrometer; SAR = Synthetic Aperture Radar.

evaporitic deposits related to lacustrine activities (Barnes et al., 2009, 2011; MacKenzie et al., 2014; MacKenzie & Barnes, 2016).

We focus our investigation on the compositional and geomorphic relationships between the first three spectral units present in the equatorial regions, meaning the IR-bright, IR-brown, and IR-blue units. The latter—the 5-μm bright units—are not being analyzed in our investigation since they do not appear to take part of the IR-bright-blue-brown contact sequence at the VIMS spatial resolution. The spectral characteristics of the three IR units identified in our composites describe an apparent transition that is consistent with compositional mixtures that may indicate they are linked by some geological processes, although their respective composition still remains enigmatic. First, we begin our analysis with the identification and mapping of the main

terrains present in the equatorial regions by using the near-IR imaging data from the Cassini spacecraft. In addition, we use the Synthetic Aperture Radar (SAR) data acquired by the RADAR instrument to retrieve the morphological properties of those terrains and look for potential correlation between both SAR features and IR units. Indeed, the dunes seen in SAR swaths appear to correspond to the IR-brown units (Rodriguez et al., 2014; Soderblom et al., 2007), while the other considered IR units (i.e., the IR-bright and IR-blue units) are linked to several geomorphologic units identified in SAR swaths (e.g., Malaska, Lopes, Williams, et al., 2016; Soderblom et al., 2007), although they are not uniquely correlated to them. In addition to the geomorphological analysis, we constrain the composition of the considered terrains by using an updated radiative transfer model to evaluate atmospheric contributions and then extract spectral information from the surface, as well as a spectral mixing model for comparison with synthetic spectra of mixtures of Titan's surface candidates. Here we assume that equatorial terrains are mainly composed of water ice and tholin-like solid organics, the two expected major components of Titan's surface. Coupling these geomorphological and compositional analyses allows us to constrain the nature of the material found in the equatorial belt of Titan and point out geological processes that could lead to the current distribution of the investigated terrains seen through VIMS and SAR data.

2. Global Mapping of the Equatorial Belt

2.1. Infrared Unit Mapping With VIMS and Imaging Science Subsystem

Cassini's VIMS acquires hyperspectral images of Titan in 352 contiguous spectral channels from 0.35 to 5.12 μm (Brown et al., 2004). Nevertheless, because of the dense atmosphere of Titan, mainly composed of methane and dinitrogen, the surface is only visible in seven narrow atmospheric windows of the near infrared while it is completely hidden in the visible. These atmospheric windows are centered at 0.93, 1.08, 1.27, 1.57, 2.01, 2.7–2.8, and 5 μm, where methane absorption is weaker (Sotin et al., 2005). These windows are still affected by a strong haze scattering, which is greater toward the shorter wavelengths and leads to a blurring effect on the observations (Rodriguez et al., 2006; Tomasko et al., 2005). Different correction methods have been developed and applied to compensate for these effects. In this study, we will use two methods: a fast semiempirical correction for IR units identification and mapping purposes (Combes et al., 1997; Cornet et al., 2012; Coustenis et al., 2001, 2005; Le Mouélic et al., 2012) and a comprehensive radiative transfer model in order to retrieve more precisely the albedo of the surface units and their composition (Hirtzig et al., 2013; Maltagliati et al., 2015; Solomonidou et al., 2014, 2016, 2018).

The semiempirical correction consists in subtracting the haze scattering additive contribution from the center of each atmospheric window, by using the wings of the window (wavelengths at which surface is not detected) as a proxy for the entire haze atmospheric scattering. Such method was initially employed to improve the visibility of ground features in images acquired by Earth-based telescopes prior the Cassini-Huygens mission (Combes et al., 1997; Coustenis et al., 2001, 2005) and then was adapted for VIMS data set (Cornet et al., 2012; Le Mouélic et al., 2012). Note that this empirical atmospheric correction is not applied for the 5-μm window, since there is little to no haze scattering in this window at first order (Rodriguez et al., 2006). The resulting radiance factor (I/F) in the atmospheric windows provides a good approximation for the surface albedo at these wavelengths. Therefore, the mapping done using a combination of simple bands or band ratios chosen within the corrected atmospheric windows allows the enhanced identification and delineation of Titan's major surface spectral heterogeneities, here called spectral units. For more details about this method, the reader is referred to Le Mouélic et al. (2012) and Cornet et al. (2012). Figure 1a is a global mosaic of Titan on which the semiempirical correction has been applied. This newly produced mosaic was oversampled at 0.38 km/pixel for mapping purposes and composed of VIMS data acquired until flyby T114 (November 2015), as described in Le Mouélic et al. (2016).

By applying this method to the VIMS data and using the color scheme previously described, we were able to accurately identify and map the "purest" spectral units present in the equatorial belt, representing about 64.3% (i.e., 53.6×10^6 km^2) of Titan's surface area. Additionally, a mosaic is produced using data collected by the Imaging Science Subsystem (ISS) at 0.938 μm with a resolution as good as 4 km, up to Titan flyby T100 (April 2014, web link: http://www.ciclops.org/view/8212/Map-of-Titan---June-2015?js=1), and is used to support the mapping of the ISS IR-dark units (comprising both VIMS IR-brown and IR-blue units; Figure 1b).

Because of the haze scattering and the fact that ISS probes the surface in a single narrow filter, ISS data do not provide compositional information but clearly reveal the spectral units with high albedo contrast, as seen by VIMS, allowing detailed mapping. The interpretative map of the equatorial belt, which we used for the selection of our regions of interest (also noted RoIs), is presented in Figure 1d.

2.2. Updated Mapping of the Widespread Dunes With the RADAR

In our study, the mapping of the major geomorphic units was performed by using SAR swaths from the RADAR instrument (Elachi et al., 2004), as done in previous studies (Birch, Hayes, Howard, et al., 2016; Lopes et al., 2010, 2016; Malaska, Lopes, Williams, et al., 2016). In SAR imaging mode in Ku-band (f = 13.78 GHz and λ = 2.18 cm), the RADAR instrument probes the surface of Titan directly through the atmosphere and provides the best spatial sampling of the remote sensing instruments onboard Cassini, with scales reaching only a few hundred meters per pixel when the spacecraft is close to Titan. Figure 1c shows the map of the equatorial belt of Titan's surface produced by gathering all the SAR swaths collected from the first Titan close flyby Ta (October 2004) to T120 (June 2016). SAR swaths have been reprojected in a simple cylindrical coordinate system using the United States Geological Survey/Integrated Software for Imagers and Spectrometers and then integrated into the ArcGIS (ESRI) software package. At the end of June 2016, 65.6% (i.e., 35.1×10^6 km^2) of Titan's equatorial belt is covered by the SAR imaging mode. The SAR swaths were used to map the dunes present on Titan's surface, the major geomorphological unit identified in the equatorial belt, which are mainly confined to the low latitudes (±40°N/S). After mapping, we evaluate that the dunes cover about 17.3% of Titan's surface mapped by SAR imaging and hence 26.8% of the equatorial belt (Figure 1d). This corresponds to a dune-covered area of about 9.5×10^6 km^2, which increases the dune areal coverage inferred from firm SAR observations by about 3×10^6 km^2 (equivalent to 10 Namib deserts on Earth) with respect to previous studies (Le Gall et al., 2011; Lopes et al., 2016; Rodriguez et al., 2014).

2.3. Updated Correlation of Infrared Units With Dunes

The IR-brown units represent 18.6% (i.e., 15.5×10^6 km^2) of the total surface area of Titan, while the IR-blue units only cover 1.5% (i.e., 1.3×10^6km^2), corresponding to 28.9% and 2.4% of the equatorial belt, respectively. The map shown in Figure 1d reveals that more than 80% of the mapped dunes correspond to IR-brown units, whereas only 2.2% are found in IR-blue units. The correlation between dunes seen in SAR swaths and VIMS IR-brown unit is thus even higher than reported in Rodriguez et al. (2014), further supporting the extrapolation of the dune material surface area to the whole geographic extent of the IR-brown unit. Therefore, the dune material coverage is assumed to be extended up to 18.6% (i.e., 15.5×10^6 km^2) of Titan's surface area (in comparison to 17.5% in Rodriguez et al., 2014).

This updated mapping of the equatorial belt enables highlighting the apparent transition from the IR-bright units to the IR-brown units, between which IR-blue units are often observed. Moreover, we demonstrated that it is necessary to compare the IR units seen in VIMS and ISS observations with the RADAR observations, in order to provide a complete description of our investigated terrains (frames in Figure 1), with the help of what was recently done in Lopes et al. (2016) and Malaska, Lopes, Williams, et al. (2016).

3. Regions of Interest Within the Equatorial Belt

The spectral and geomorphologic global mapping of the equatorial regions presented above allows us to identify regions where IR-bright, IR-brown, and IR-blue units are in contact. We study several areas such as Sinlap crater (16°W, 11°N), Aaru Regio (350°W, 5°N), Menrva crater (87°W, 20°N), Eastern Xanadu province (55°W, 10°S), and Chusuk Planitia (23°W, 4.5°S). The locations of these regions are indicated in Figure 1, while Table 1 reports their VIMS and RADAR viewing conditions.

3.1. Sinlap Crater

Sinlap is a relatively fresh crater with a diameter of about 80 km, centered at 16°W and 11°N. At a regional scale, Sinlap crater was observed by VIMS during flyby T13 in April 2006 with a spatial sampling of about 14 km/pixel (cube CM_1525118253 in Figure 2a with red: 1.57/1.27 μm, green: 2.01/1.27 μm, and blue: 1.27/1.08 μm). These images show that the whole crater area is surrounded by the Fensal sand sea, as seen in green in the semiempirically corrected VIMS false-color band ratio composites (Figures 2a and 2b). For consistency with previous studies, the green area in Figures 2a and 2b is referred to the IR-brown dune

Table 1
VIMS Cube Observations and RADAR/SAR Swaths Used for Our Investigation

Data set/flyby	PDS label	Date	Incidence (deg)	Emission (deg)	Phase (deg)	Altitude (km)	Spatial sampling (km/pixel)	Exposure time (ms)
			Sinlap crater					
VIMS T13	CM_1525118253	April 2006	30–47	0–20	40–42	26,790	14	68
VIMS T105	CM_1790056808	September 2014	20–24	20–48	35–59	3,057	1.5	160
VIMS T109	CM_1802454074	February 2015	25–31	0–32	21–29	3,158	1.6	220
VIMS T110	CM_1805209469	March 2015	23–30	18–27	35–37	6,222	3.1	70
SAR T3	BIBQI22N068_D045_T003S01	February 2005	4–30	—	—	1,579	0.17	—
			Aaru regio					
VIMS T61	CM_1629905033	August 2009	9–40	8–47	11–13	27,588	13.8	80
VIMS T109	CM_1802450543	February 2015	9–30	18–49	41–44	24,248	12.1	90
SAR T23	BIBQI26N009_D111_T023S01	January 2007	9–38	—	—	1,000	0.17	—
SAR T104	BIBQG03S348_D261_T104S02	August 2014	41–75	—	—	964	0.7	—
SAR T108	BIBQG01N352_D265_T108S02	January 2015	10–60	—	—	970	0.7	—
			Menrva crater					
VIMS T114	CM_1826075655	November 2015	7–71	2–87	28–30	62,378	34	320
	CM_1826086162		36–52	21–38	56–64	15,177	7.6	140
SAR T3	BIBQI22N068_D045_T003S01	February 2005	4–30	—	—	1,579	0.17	—
SAR T77	BIBQI10N064_D229_T077S01	June 2011	8–32	—	—	1,359	0.17	—
	BIBQG11N071_D229_T077S03		39–71	—	—	1,359	0.7	—
			Eastern Xanadu					
VIMS T9	CM_1514313117	December 2005	2–21	1–27	21–28	17,532	8.7	160
	CM_1514315913		14–26	34–58	59–70	11,182	5.6	80
VIMS T114	CM_1826082135	November 2015	28–55	0–24	33–36	32,165	16	280
	CM_1826085255		38–53	10–17	46–52	18,143	9	280
SAR T113	BIBQI10S066_D271_T113S01	September 2015	5–64	—	—	1,036	0.17	—
			Chusuk Planitia					
VIMS T20	CM_1540485266	October 2006	13–15	2–41	10–44	1,321	0.6	80

Note: In SAR imaging mode, the source of illumination is the antenna itself. Altitude refers to the altitude at the closest approach during the Cassini flyby. There are no SAR swaths crossing Chusuk Planitia. VIMS = Visual and Infrared Mapping Spectrometer; SAR = Synthetic Aperture Radar; PDS = Planetary Data System.

areas (color initially found in RGB color composites of uncorrected bands and band ratios in numerous publications). The crater floor appears to be filled by IR-blue materials and is surrounded by a ring of IR-bright materials corresponding to the main ejecta blanket, Bazaruto Facula. A large halo with a low albedo and a blue appearance in the false-color composites is oriented southeastward and is encircling the IR-bright ejecta blanket. In Le Mouélic et al. (2008), this IR-blue plume-shaped and dune-free area is suggested to be a sheet of icy deposits originated by a water vapor plume produced during the impact. Moreover, Solomonidou et al. (2014) applied the Principal Component Analysis technique in order to calculate color units that each correspond to a unique spectral signature in the same VIMS cube as in Le Mouélic et al. (2008) and obtained the same results of three distinct regions.

Figure 2b is a projected mosaic of three more recent VIMS high-resolution observations displayed with the same color scheme as in Figure 2a. The first observation was taken during the flyby T105 in September 2014 with a spatial sampling of about 1.5 km/pixel (cube CM_1790056808). The second observation was recorded during the flyby T109 in February 2015 with a spatial sampling of about 1.6 km/pixel (cube CM_1802454074). The last observation used for this mosaic was taken 1 month later during the flyby T110 (March 2015), with a spatial sampling of about 3.1 km/pixel (cube CM_1805209469). The first observation, from flyby T105, was analyzed in Neish et al. (2015) to provide further morphological details about Sinlap's region at local scale, while the two other observations (T109 and T110) have not been studied and published so far. This mosaic (Figure 2b) reveals a degraded central peak, which is as bright as the main ejecta blanket of the crater. Numerous dark linear features are seen embedded in the ejecta blanket that can be interpreted as channels (Neish et al., 2015), but some of them seen in the southern part of the blanket could even be post-impact fractures since they clearly appear alongside the crater flanks (not radially) in both VIMS and RADAR observations. Additionally, there is evidence of IR-brown sand material within the crater floor that is spectrally similar to that of the dunes, although no dunes are seen. As shown in Figure 2c, Sinlap crater and its surroundings have been observed by the RADAR instrument in SAR imaging mode during the flyby T3 (February 2005),

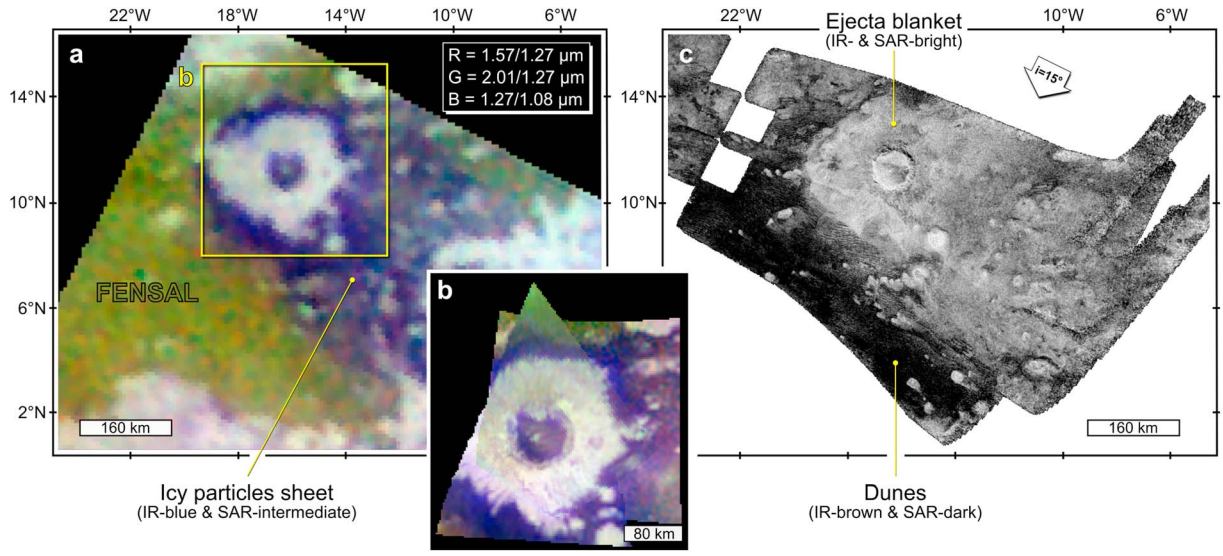

Figure 2. Sinlap crater and its surroundings (16°W, 11°N). (a) Visual and Infrared Mapping Spectrometer (VIMS) false-color composite of band ratios from flyby T13 (April 2006). (b) Mosaic of the three VIMS observations from flybys T105 (September 2014), T109 (February 2015), and T110 (March 2015; red: 1.57/1.27 μm, green: 2.01/1.27 μm, and blue: 1.27/1.08 μm). (c) SAR swath from flyby T3 (February 2005) targeting Sinlap crater (same scale as a) with a spatial sampling of 170 m/pixel. The VIMS observations are oversampled with a scale of about (a) 6 km/pixel and (b) 1 km/pixel and are empirically corrected from haze backscattering. All images are displayed in simple cylindrical projection, and north is up. The white arrow in (c) indicates the RADAR illumination. SAR = Synthetic Aperture Radar.

with a pixel scale reaching 170 m/pixel, clearly revealing dunes, as long dark linear streaks, within the surrounding sand sea. While a clear difference appears between the IR-bright and IR-blue units in the VIMS false-color composites, these regional infrared differences are not seen in the SAR swaths, which may imply that the IR-blue unit in this area is quite superficial.

3.2. Aaru Regio

Aaru is a large region with mixed low and intermediate albedo confined at 5°S to 15°N, and 330°W–360°W, which can be considered as an extension of the Senkyo sand sea. VIMS acquired observations of this region at medium scale (around 13.8 km/pixel) during the flyby T61 (August 2009 in Figure 3a). Aaru Regio is essentially seen in the VIMS observation cube labeled CM_1629905033 (Buratti et al., 2012). A second observation, unpublished yet, was acquired later during flyby T109 (February 2015) with a higher spatial sampling at 12.1 km/pixel (cube CM_1802450543). Moreover, SAR and HiSAR (standing for High Altitude SAR) swaths are crossing the region at high and medium samplings (from 700 to 170 m/pixel), with swaths collected during flybys T23 (January 2007), T104 (August 2014), and T108 (January 2015; Figure 3b). The northwestern area of Aaru Regio is surrounded by IR-bright units that are locally bright in the SAR swaths, which implies a rough surface at the RADAR wavelength, such as Handir Colles (356.7°W, 10°N in Figure 3c). Furthermore, some areas appear blue in the VIMS false-color composite. They are devoid of dunes, featureless, and display an intermediate brightness in SAR swaths, which is likely to be due to a greater roughness and volume scattering than surrounding terrains. One of these IR-blue areas seems to be enclosed between IR-bright units and IR-brown dune areas, such as the Giedi Planitia located at 358°W, 7°N (Figure 3d). Figure 3e shows that the region is hosting a 120-km diameter impact crater, named Paxsi (341.2°W, 5°N), with strongly breached rims and a central pit. Paxsi's rims are degraded enough to let the dunes fill in, as mentioned in Buratti et al. (2012) and Hofgartner et al. (2016). We cannot assess the presence of channels at the resolution of the observations.

3.3. Menrva Crater

The third region investigated in this study is centered on Menrva crater (87°W, 20°N), the largest impact crater on Titan with a diameter of about 400 km. VIMS acquired the best spatially resolved observations of this region during flyby T114 (November 2015). Those new observations were registered at both relatively low (about 34 km/pixel, Figure 4a) and moderate (about 7.6 km/pixel, Figure 4c) spatial sampling. Figure 4b is a mosaic of SAR swaths crossing the region, with a close-up in Figure 4d. While the SAR swath from flyby T3 (February 2005) was crossing a small part of the crater, the swaths from flyby T77 (June 2011) almost cover the whole region. This large crater is a heavily eroded, double-ringed impact basin, as described in Wood

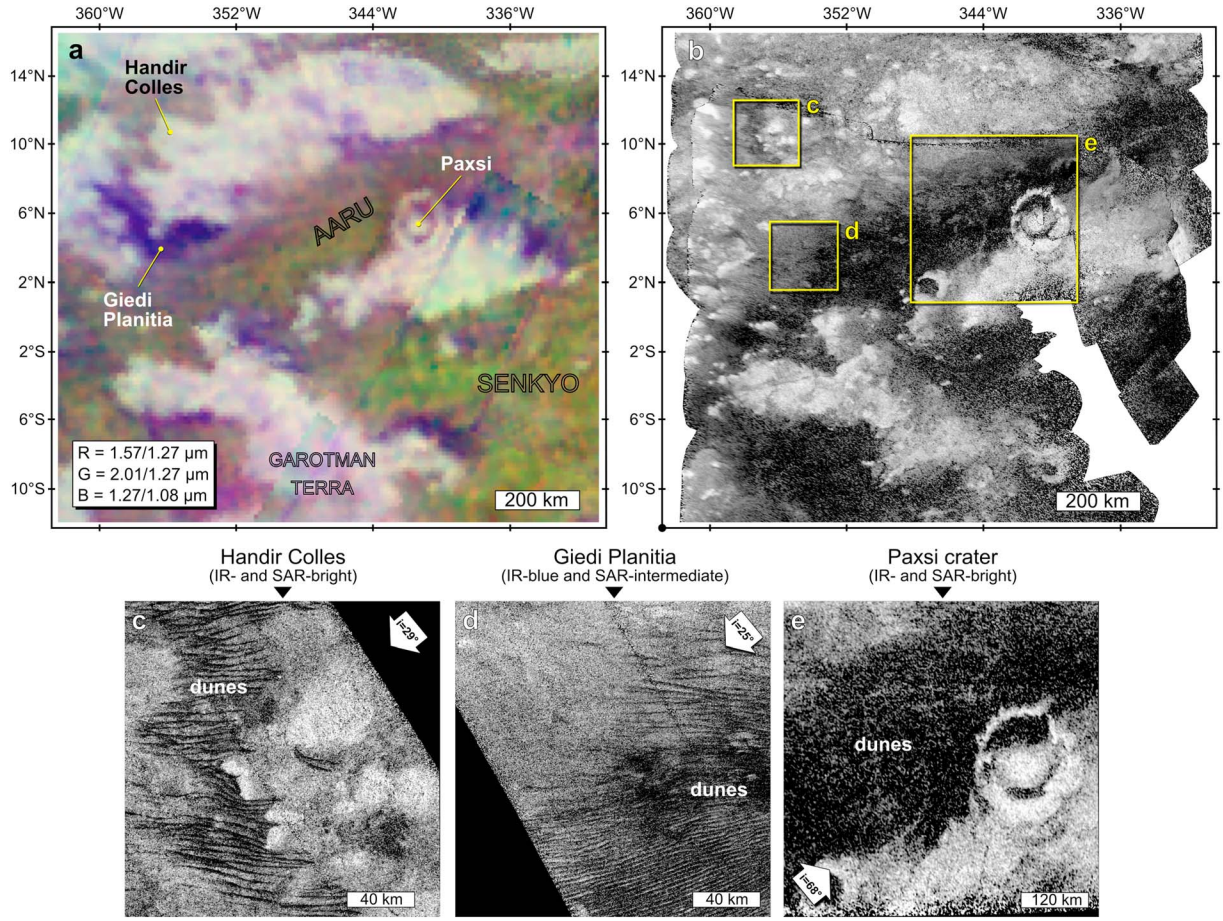

Figure 3. Aaru Regio (350°W, 5°N). (a) Visual and Infrared Mapping Spectrometer (VIMS) false-color composite of band ratios from T61 (red: 1.57/1.27 μm, green: 2.01/1.27 μm, and blue: 1.27/1.08 μm), taken in August 2009. This composite is oversampled at 10 km/pixel and is empirically corrected from haze backscattering. (b) Combined SAR swaths from flybys T104 and T108 at λ = 2.18 cm, taken in August 2014 and January 2015, respectively (700 m/pixel). Images (a) and (b) are displayed at the same scale. (c) Closer up on Handir Colles, an IR-and SAR-bright area as mountainous-like terrains. (d) IR-blue and SAR-intermediate Giedi Planitia as a dune-free area. (e) IR- and SAR-bright Paxsi crater, as well as the IR-brown and SAR-dark dunes. Paxsi crater (120-km diameter) displays breached rims and dunes filling in. Images (c) and (d) are derived from SAR swaths taken during flyby T23 (January 2007, at 170 m/pixel), while image (e) was acquired during flyby T108 (January 2015), at 700 m/pixel. All images are displayed in a simple cylindrical projection, and north is up. The white arrows in (c), (d), and (e) indicate the RADAR illumination. SAR = Synthetic Aperture Radar.

et al. (2010) and Williams et al. (2011). Numerous SAR-bright channels start near the rim crest and flow eastward away from the crater, crossing the ejecta blanket and a large SAR-bright area of probable deposited material, named Elivagar Flumina (top right corner in Figure 4e). The channels all end up in a large fan-like area, one of the SAR-brightest areas of the region, as bright as the channels themselves, and are referred as an alluvial or fluvial fan (Birch, Hayes, Dietrich, et al., 2016; Radebaugh et al., 2016). This fan-like area is strongly correlated with the IR-blue unit seen in the VIMS false-color composite in Figure 4c and also discussed in Radebaugh et al. (2016). The inner ring within Menrva crater shows SAR-bright knobs that are also bright in the near-IR data. The floor between the outer and inner rims of Menrva is dark in the SAR swaths and is therefore relatively smooth at the RADAR wavelength. This area seems to contain a few dark streaks southeast of the crater that are probably dunes. Unfortunately, the resolution of the VIMS observations does not allow distinguishing whether these dunes are found in IR-brown or IR-blue units or possibly in both.

3.4. Eastern Xanadu and Chusuk Planitia

The last region we selected covers the Aztlan sand sea, forming a corridor of dunes starting from the oriental part of Xanadu to Aaru Regio, that is, from 0°S to 20°S and from 0°W to 70°W. Two areas were selected in this vast region for our study: eastern Xanadu and Chusuk Planitia, as shown in Figure 5.

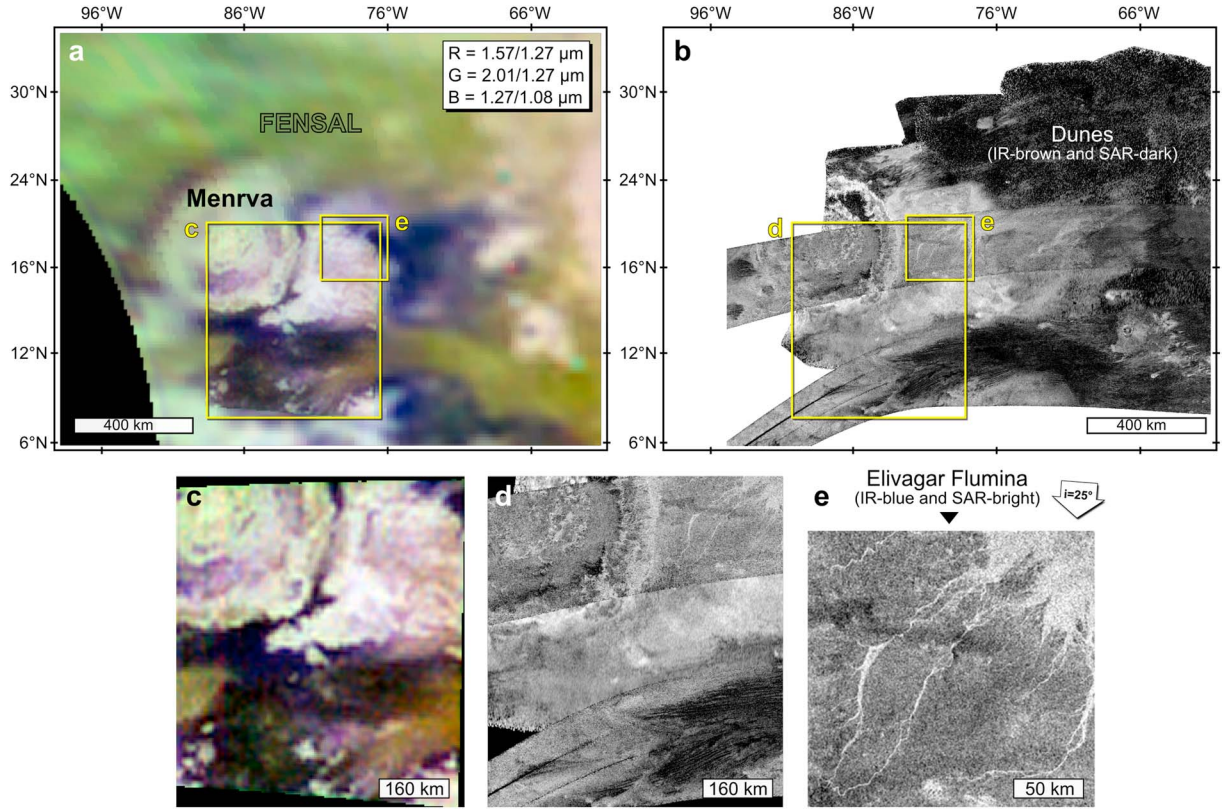

Figure 4. Menrva crater and its surroundings (87°W, 20°N) as seen, for the first time, in Visual and Infrared Mapping Spectrometer (VIMS) false-color composites of band ratios (red: 1.57/1.27 μm, green: 2.01/1.27 μm, and blue: 1.27/1.08 μm) from flyby T114 (November 2015), at (a) regional-scale and at (c) higher resolution. These new VIMS observations are oversampled with a spatial sampling of about (a) 10 km/pixel and (c) 3 km/pixel and are empirically corrected from haze back-scattering. (b) Mosaic of SAR swaths from flybys T3 (February 2005) and T77 (June 2011), with a spatial sampling varying from 700 to 170 m/pixel (same scale as [a]). (d) Close-up of the SAR mosaic in (b), at the same location and scale of (c). (e) Close-up of the IR-blue and SAR-bright dry fluvial network named Elivagar Flumina, through SAR swath T3. All images are displayed in a simple cylindrical projection, and north is up. The white arrow in (e) indicates the RADAR illumination. SAR = Synthetic Aperture Radar.

The eastern part of the IR-bright Xanadu province was first observed at relatively high resolution by VIMS during flyby T9 (December 2005). New observations of this region have been collected by VIMS during the flyby T114 (November 2015 in Figure 5a). Features described as branching, dark, and curvilinear are seen in Xanadu and are interpreted as channels in Barnes, Radebaugh, et al. (2007). These IR-blue channels are inferred to represent surface runoff channels that drain the IR-bright region into the surrounding IR-blue unit, westward of the IR-brown dune areas Aztlan and Fensal. In addition to these channels, IR-bluish patches are found within the IR-bright Xanadu, as also mentioned in Barnes, Radebaugh, et al. (2007). As shown in Figure 5b, those embedded IR-blue patches correspond to SAR-bright patches, suggesting rough and possibly mountainous terrains. Conversely, the IR-bright surroundings exhibit a homogeneous SAR-dark appearance similar to that of plains (Lopes et al., 2016; Malaska, Lopes, Williams, et al., 2016). The SAR swath shown in Figure 5b was acquired during flyby T113 (September 2013) and illustrates the contrast between the IR-bluish patches and channels (SAR-bright) and the IR-bright surroundings (SAR dark).

Finally, Chusuk Planitia was described as a dark indentation within the IR-bright Quivira plateau (Jaumann et al., 2008). Hence, this region marks the transition between IR-bright and IR-blue units and farther southward the IR-brown dunes from Aztlan sand sea. As shown in Figure 5c, Chusuk Planitia was observed by VIMS during flyby T20 in October 2005 (cube CM_1540485266) with an averaged spatial sampling of around 0.6 km/pixel. Since Chusuk Planitia is found in an IR-blue area, it was suggested to be covered by debris that have been transported after fluvial incision in the IR-bright units (Jaumann et al., 2008). The absence of SAR swath in this region does not allow us to state whether or not dunes are present in Chusuk Planitia.

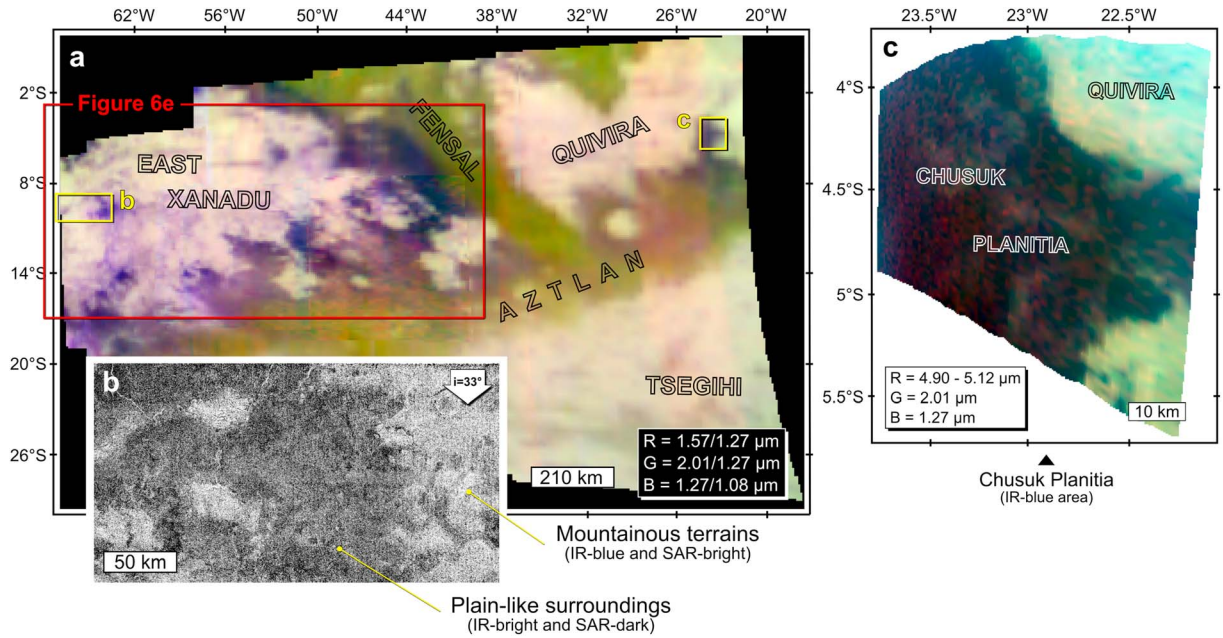

Figure 5. Eastern Xanadu (55°W, 10°S) and Chusuk Planitia (23°W, 4.5°S). (a) Visual and Infrared Mapping Spectrometer (VIMS) false-color composite of band ratios covering Aztlan region from the recent flyby T114 (November 2015; red: 1.57/1.27 μm, green: 2.01/1.27 μm, and blue: 1.27/1.08 μm). (b) Close-up within the eastern part of Xanadu province through SAR swath from T113 (September 2015), displaying the SAR-bright and IR-blue mountains terrains, in contrast to the SAR-dark and IR-bright surroundings. (c) Chusuk Planitia as seen in VIMS observation acquired during flyby T20 (October 2006; red: average over 4.90–5.12 μm, green: 2.01 μm, and blue: 1.27 μm). The VIMS observations are oversampled with a spatial sampling of about (a) 6 km/pixel and (c) 0.3 km/pixel, respectively, and are empirically corrected from haze backscattering. All images are displayed in a simple cylindrical projection, and north is up. The white arrow in (b) indicates the RADAR illumination. The red frame in (a) indicates the location of Figure 6e. SAR = Synthetic Aperture Radar.

3.5. Observation Summary

Figure 6 displays interpretative maps of the regions considered through optical and microwave observations that disclose the IR units as well as the discernible morphologies (i.e., dunes and channels) seen in SAR swaths. Additionally, Table 2 summarizes all those morphologies and their potential correlation with each IR unit present in our investigated regions. This illustrates that IR units, despite specific spectral characteristics, do not systematically correspond to one type of SAR brightness unit, especially in terms of roughness and volume scattering, and thus cannot be unequivocally associated with one type of surface feature. Rather, correlation highly depends on the local geological context. For example, the IR-blue units can be found in SAR-bright patches (corresponding to potential local topographic highs) and channels within large IR-bright units and also in SAR-intermediate and featureless plain-like terrains at the edges of IR-bright units.

The interpretative maps shown in Figure 6, combined with the chemical characterization of the three IR units (bright, blue, and brown; section 4), will allow us to propose a scenario for the formation of each of those terrains, as well as possible explanations for their geological connections (section 5).

4. Constraints on Infrared Units' Composition

4.1. Description of the Radiative Transfer Model

We applied a radiative transfer model in order to evaluate the atmospheric effects (gases absorption and haze scattering) on the observed spectra and retrieve the surface albedo of the IR units. The model was developed by Hirtzig et al. (2013) and is based on the plane-parallel version of the Spherical Harmonics Discrete Ordinate Method solver (Evans, 2007). It divides Titan's atmosphere into 70 layers from 700-km altitude to the surface. Most of the inputs feeding the solver are given by in situ measurements made by Huygens' instruments during the descent of the probe in January 2005. The vertical profiles of the pressure (*P*), temperature (*T*), and molar mass are obtained from the Huygens Atmospheric Structure Instrument (Fulchignoni et al., 2005). The atmospheric inputs include several gases (CH_4, $^{13}CH_4$, CH_3D, N_2, CO, and C_2H_2) that produce molecular and collision-induced absorptions as well as Rayleigh scattering. Gas

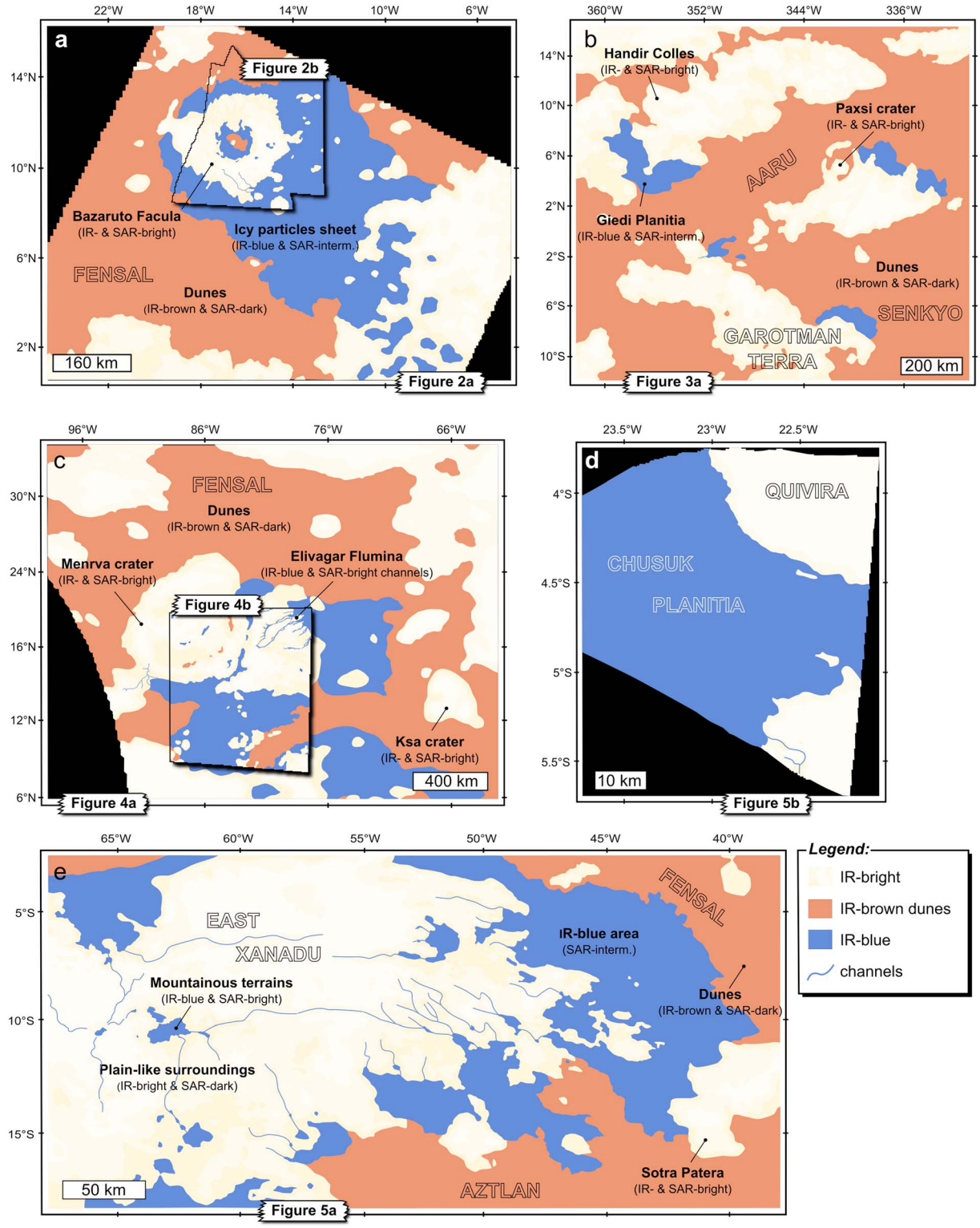

Figure 6. Geological interpretation of the regions of interest made on the basis of spectral and roughness (and/or volume scattering) variations in both data sets (Visual and Infrared Mapping Spectrometer and RADAR/Synthetic Aperture Radar), for (a) Sinlap crater, (b) Aaru Regio, (c) Menrva crater, (d) Chusuk Planitia, and (e) Eastern Xanadu region. Annotations referring to the original images used for mapping are displayed on each map.

Table 2
Correlations Between the IR Units and SAR features

IR units	SAR backscatter	Landforms	References
IR-bright			
	Moderate to low	Plains (undifferentiated and variables units)	Lopes et al. (2016) and Malaska, Lopes, Williams, et al. (2016)
	High	Mountainous terrains, and craters (ejecta, rims and central peaks)	Lopes et al. (2016) and Malaska, Lopes, Williams, et al. (2016)
IR-blue			
	Moderate	Featureless, plain-like areas, and halos surrounding craters	Le Mouélic et al. (2008) and Jaumann et al. (2010)
	High	Channels and isolated patches in mountainous terrains	Barnes, Radebaugh, et al. (2007) and Soderblom et al. (2007)
IR-brown			
	Low (streak-shaped)	Dunes	Soderblom et al. (2007) and Rodriguez et al. (2014)

Note. SAR = Synthetic Aperture Radar.

abundance vertical profiles were measured by the Huygens/Gas Chromatograph Mass Spectrometer (CH_4 from Niemann et al., 2010) and the Cassini/Composite Infrared Spectrometer (CO from de Kok et al., 2007; C_2H_2 from Vinatier et al., 2010). The optical properties of the aerosols, namely, the single-scattering albedo, the opacity, and the phase function, are inherited from the Huygens/Descent Imager Spectral Radiometer (DISR) measurement analysis in the visible and near-IR ranges (Tomasko et al., 2008) and from laboratory experiments (Khare et al., 1984), as well as adjustment to VIMS data (Hirtzig et al., 2013) in the IR range. However, the DISR data only provide constraint up to 1.6 μm and the aerosols properties inferred at longer wavelengths are therefore an extrapolation of the results. The radiative transfer model assumes a Lambertian surface. This particular scattering behavior of the surface has been locally reported by Schröder and Keller (2008), when analyzing the Huygens/DISR data acquired during the last stages of the module descent. Interestingly, the same behavior seems to apply at broader scale on Titan, since the analysis of the surface photometry in the 5-μm window (the least affected by atmospheric effects), using a global mosaic VIMS data acquired between Ta and T70, revealed a strong correlation between the brightness of the surface at 5 μm and the Lambert cosine factor (Le Mouélic et al., 2012). The reader is referred to Hirtzig et al. (2013) and Solomonidou et al. (2014) for further explanation, more details, and additional references on the radiative transfer model. This model has already been used to extract surface and atmospheric information for several Titan surface regions (Solomonidou et al., 2014, 2018), search for temporal surface and haze changes (Solomonidou et al., 2016), and compare among various geomorphological units (Bonnefoy et al., 2016; Lopes et al., 2016).

Although a radiative transfer model is an effective tool to retrieve surface properties, it is generally time-consuming. We therefore do not apply this model to invert directly the VIMS cubes, as for classical approaches, but we compute and interpolate solutions on a reference lookup table (LUT), as described in Maltagliati et al. (2015). The LUT is produced using the radiative transfer model as a forward model for different values of input and output parameters: the solar incidence, emergence, phase angles, and two output physical characteristics (haze total opacity and surface albedo). This method can simultaneously retrieve maps of relative opacity of haze with respect to the opacity at the Huygens landing site in January 2005, and surface albedo in the seven atmospheric windows, in a few minutes (for an usual 64 × 64 cube), in comparison to the several (tens of) days needed with a classical inversion with the full radiative transfer model. Since the model assumes a Lambertian surface, the surface albedo we retrieve is in fact a Lambert surface albedo (noted A_L), corresponding to the hemispheric reflectance of an isotropically scattering surface (Hapke, 2012).

This inversion with the LUT has been applied to all the VIMS cubes listed in Table 1. For each of these cubes (representing in total more than 50,000 spectra), we thus obtained maps of Lambert albedo of the surface in the eight infrared atmospheric windows (see supporting information Figures S1 to S4). In order to dispense with the highly variable observation geometries and for the ease of comparison, we then convert the output Lambert surface albedo into single-scattering albedo (ω_0), following the Hapke (2012) formalism in the case of an isotropic scattering and compacted medium. Finally, we use masks in our regions of interest (RoIs) to extract surface single-scattering albedo information for each of the spectral units, namely, IR-bright, IR-blue, and IR-brown units, found within each of the selected cubes (see supporting information Figure S5).

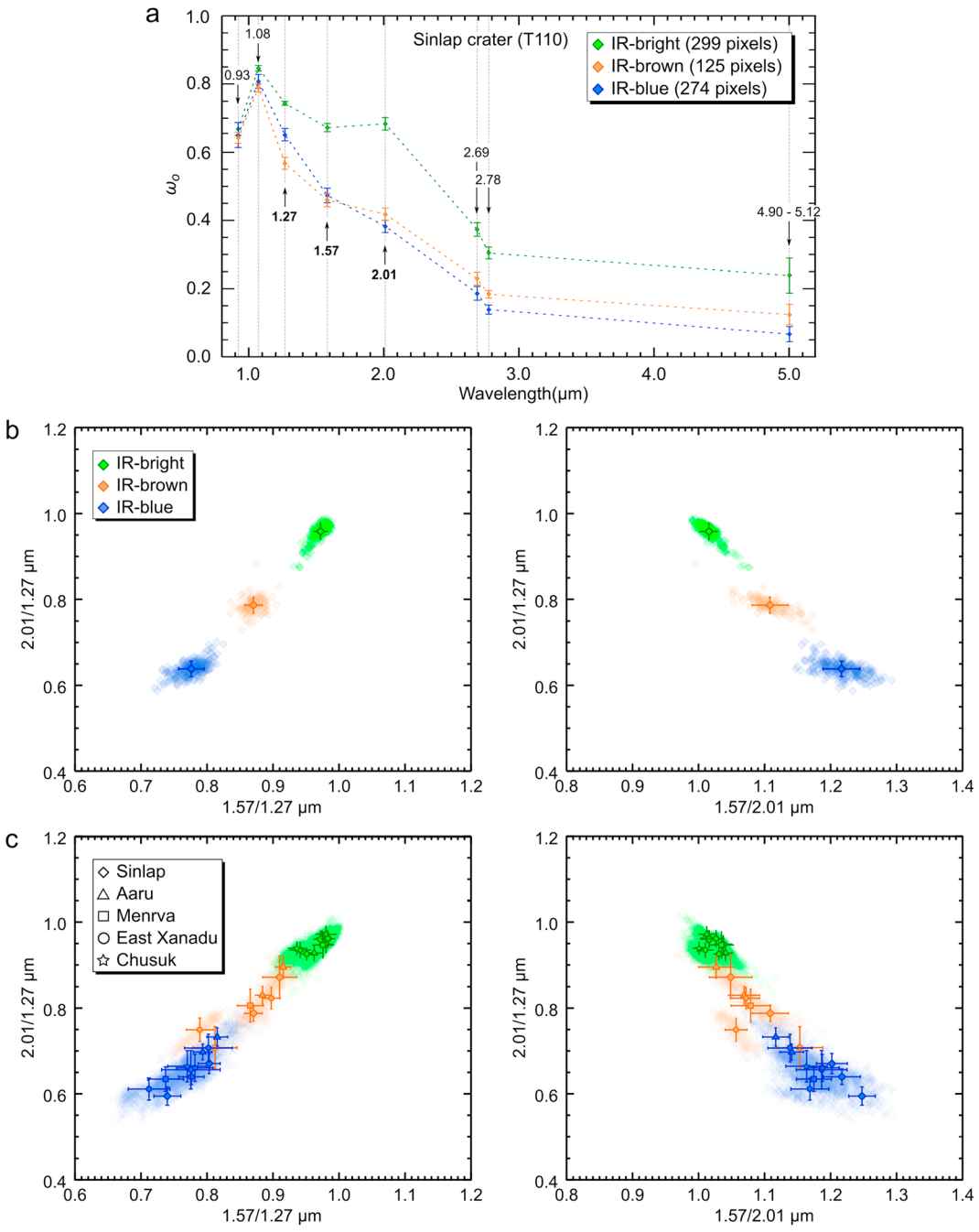

Figure 7. Top row: (a) spectra of the averaged single-scattering albedo (ω_0) in the eight infrared atmospheric windows for all the pixels comprised in each region of interest (RoI) of the Visual and Infrared Mapping Spectrometer (VIMS) observation targeting the Sinlap crater area (T110, CM_1805209469), as an example illustrating the spectral distinct characteristics of each IR unit: IR-bright (green plots), IR-brown (brown plots), and IR-blue (blue plots) units. The number of pixels comprised in the RoIs is indicated in the top right corner of the plot. Middle and bottom rows: Scatterplots of the (left) 1.57/1.27 μm versus 2.01/1.27 μm and (right) 1.57/2.01 μm versus 2.01/1.27 μm spectral slopes for the IR units. The spectral slopes are calculated from the single-scattering albedo spectra retrieved with the radiative transfer model (see text for details). Those are the results obtained for (b) the Sinlap crater area through the VIMS observation from flyby T110 and (c) all the investigated regions (all RoIs): Sinlap crater (diamonds), Aaru Regio (triangles), Menrva crater (squares), eastern Xanadu province (circles), and Chusuk Planitia (stars). Error bars are the standard deviation.

4.2. Spectral Slopes Comparison

Figure 7a shows spectra of the single-scattering albedo in the seven atmospheric windows, calculated from the radiative transfer model for the IR units found in Sinlap crater and its surroundings. Spectra obtained for each region investigated are provided in the supporting information (see Figure S6). The spectral differences

between the various IR units on Titan essentially appear at the short wavelengths, using the 1.27-, 1.57-, and 2.01-μm window images (Rodriguez et al., 2006). We therefore decided to extract and compare the spectral slopes of the single-scattering albedo between these windows, that is, 1.57/1.27, 2.01/1.27, and 1.57/2.01 μm, for the three IR units identified in our RoIs. Spectral slopes are particularly sensitive to subtle heterogeneities in the composition and physical structure of the surface material (e.g., Mustard & Sunshine, 1999).

Scatter plots displayed in Figure 7b show an example for the results obtained for Sinlap crater and its surroundings as observed during the T110 flyby. The three IR units cluster in different regions of the spectral slope space. This strongly suggests that (1) each unit has intrinsically a relatively uniform spectral behavior and (2) they represent significant distinctions in spectral behaviors between them, which suggest that they are likely to differ in composition and/or grain size. Although data reduction (calibration errors, data noise, and systematic errors of the model) leads to some residual (calculated to be less than 20% on the spectral slope values), differences in the spectral slopes derived from distinct VIMS cubes are mainly due to global variability. However, Figure 7c, which represents the same plots for all our RoIs, illustrates the more "transitional" behavior of the units at global scale. When comparing the 1.57-/1.27-μm spectral slope as a function of the 2.01-/1.27-μm spectral slope (left column in Figures 7b and 7c) and the 1.57-/2.01-μm spectral slope as a function of the 2.01-/1.27-μm spectral slope (right column in Figures 7b and 7c), we observe a consistent trend in which the IR-blue unit has the lowest 1.57-/1.27-μm ratio and 2.01-/1.27-μm ratio and the highest 1.57-/2.01-μm ratio. Conversely, the IR-bright unit shares the highest 1.57-/1.27-μm ratio and 2.01-/1.27-μm ratio and the lowest 1.57-/2.01-μm ratio.

4.3. Spectral Mixing Model

For comparison purposes, we use a spectral mixing model to generate a spectral library for linear binary mixtures of water ice and tholins (Hapke, 2012). We vary the grain sizes (from 50 nm to 1 mm in diameter) and the mixing fraction (from 0% to 100%) of the two components. Owing to the low spatial resolution of our observations, linear (also referred as areal) mixing is assumed to be the best suited effect occurring for capturing natural surface heterogeneities (Villa et al., 2011), and nonlinear mixing is therefore not considered in our investigation.

The choice for mixtures of two-component endmembers seems to be the best compromise between reducing at a reasonable level the modeling complexity and the number of free parameters and at the same time keeping the best plausible representability of major surface candidates. Using such a mixing model allows to estimate the main contributors to their infrared spectra rather than deriving a precise composition. Another interesting advantage of this method, as the infrared range is very sensitive to granulometry, is to provide also an evaluation of the grain size range for each of the components of the mixture, which could bring valuable information on the local geology, as soon as their optical constants are known in the desired spectral range and temperatures.

To date, all observation attempts from Earth-based telescopes and Cassini's VIMS to determine Titan's surface major component(s) suggest that the surface is spectrally heterogeneous. The dominant and most plausible candidate is "dirty" water ice, implying that water ice is mixed with complex solid organics whose composition would be close to tholin-like materials, laboratory analogs of Titan's photochemical aerosols (Khare et al., 1984), settling from the atmosphere (Coustenis et al., 1995, 2001, 2005; Griffith et al., 1991, 2003, 2012; McCord et al., 2006, 2008; Negrão et al., 2006; Rodriguez et al., 2006, 2014). As for the water ice, it is thought to be present in the near surface of Titan, since it primarily forms the first hundred kilometers of the crust (Fortes, 2012; Sohl et al., 1995; Tobie et al., 2005, 2006). A few heterogeneities, in particular among the infrared darkest units, have been suggested to be attributed to a local enrichment in droplets of liquid hydrocarbons in order to darken the surface (Coustenis et al., 2005; Hirtzig et al., 2005). Unfortunately, spectra recorded by the Huygens/DISR instrument do not solve the problem, even locally. Apart from a single shallow absorption feature at 1.5 μm, the evidence for pure water ice is rather inconclusive, as part of the spectra recorded by Huygens is rather consistent with organic material (Tomasko et al., 2005; Schröder & Keller, 2008). Besides, analysis of VIMS spectra, in the infrared atmospheric windows, has completely ruled out the exposure of resolved water ice-dominated materials on Titan, at least at a global scale, and has possibly identified some organics at a few places in low albedo areas (Clark et al., 2010). However, Rannou et al. (2016) recently tested the hypothesis of the presence of a moist soil at the Huygens landing site, as locally measured by the Huygens/Gas Chromatograph Mass Spectrometer instrument (Niemann et al., 2010), whose spectrum

is successfully explained by a layer of water ice grains covered with aerosol aggregates wetted by liquid methane. Despite a better agreement between the model and the Huygens measurements, the shape of the spectrum is still not fully reproduced.

For our study, we chose to use binary linear mixtures of water ice and laboratory tholins. Synthetic spectra of the single-scattering albedo of both candidates are computed from their optical constants (n, k) inferred at 90 K (Grundy & Schmitt, 1998; Khare et al., 1984), by using the Mie theory for grain size equivalents or smaller than the wavelength and the equivalent slab model formalism developed by Hapke (2012) for larger grain sizes. The choice of tholins is both driven by the previous literature and the fact that other potential relevant candidates produced higher in the atmosphere (Krasnopolsky, 2009, 2014; Lavvas et al., 2008a, 2008b; Willacy et al., 2016) recombine to form larger molecules at lower altitudes, potentially similar to laboratory tholins. Besides, the optical constants (n, k) of these "simpler" organics are not always available in the literature for the right state, wavelength range, and temperatures. Note that optical constants of various tholins exist in the literature depending on the initial gas composition in the experiments (Brassé et al., 2015; Cable et al., 2012), but those determined by Khare et al. (1984) allow to cover the entire VIMS wavelength range at once. We determine that the transition between both regimes occurs at $(n_r - 1).X \sim 0.6$ both for water ice and tholins, with n_r the real part of the refractive index and $X = \pi D/\lambda$ the size parameter (D being the grain diameter and λ the wavelength). The $(n_r - 1).X$ factor for which we switch between Mie and Hapke theories has been inferred by minimizing the absolute difference (below 0.1%) between single-scattering albedo spectra calculated from the two theories.

For every pixel (10,576 in total) of the selected spectral units in our RoIs, we then search for the linear binary mixture (varying water ice/tholins mixing factor and grain size of each component) that simultaneously best reproduces the combined single-scattering albedo in each of the 1.27-, 1.57-, and 2.01-μm windows (expressed in ω_0) retrieved from the observations. We select the best solution among all the possible solutions that conservatively matches a 5% total relative difference between the observations and the model. Figure 8 displays the best solutions for our RoIs selected within the IR-bright, IR-blue, and IR-brown units (from left to right column, respectively). A summary can also be found in Table 3. Additional details about the validation of the method to retrieve surface properties are given in the supporting information (see Figure S7). It is worth noting that we are simultaneously constraining the mixing ratio of water ice and tholins as well as their respective grain sizes with surface albedos at the center of only three atmospheric windows. Among the eight atmospheric windows available in VIMS data, only surface albedo estimations at the 1.27-, 1.57-, and 2.01-μm windows are the most reliable using the radiative transfer model described above. Indeed, although haze scattering is much lower at long wavelengths relative to short wavelengths, there are substantial uncertainties in the spectral properties of the haze (whose single-scattering albedo is poorly known beyond 2.5 μm for instance). Besides, the methane absorption coefficients used in this study are also subject to large uncertainties below 1.2 μm. We consequently do not include these wavelengths in the present study and acknowledge that although we verified that our results are robust over a broader range of wavelengths, including further wavelengths for the inversions (once better constraints will be implemented in the radiative transfer model) could lead to a better evaluation of the surface albedos (consequently of the mixing states and grain sizes) and therefore to slight deviations from the trends we draw in this paper.

Considering the results for our linear mixing model, statistically, the IR-bright unit appears to be largely dominated by fine-grained tholins (80% of the mixture), of a few tens of microns (~25 μm in average), with a residual amount of large-grained water ice (possibly greater than our largest size of 1 mm in Figure 8, left column). In addition, our linear mixing model shows a possible contribution of smaller water ice grains for a few spectra (~15%) of the IR-bright RoIs, all dominated by the presence of tholins.

Our linear binary mixing model finds a solution for all the pixels in the RoIs of the IR-blue units. Interestingly, the IR-blue unit is characterized by significant water ice enrichment relative to the other units, with 60% of tholins in average (Figure 8 middle column). The water ice component presents a grain size distribution that is slightly broader than for the IR-bright unit, starting with grains of a few hundreds of microns and reaching millimeter-sized grains. Our inversions show a possible contribution of submicronic water ice for a few spectra (~20%) of the IR-blue RoIs. The tholin component shows a grain size distribution ranging from a few tens to hundreds of microns (~50 μm in average in Figure 8, middle column).

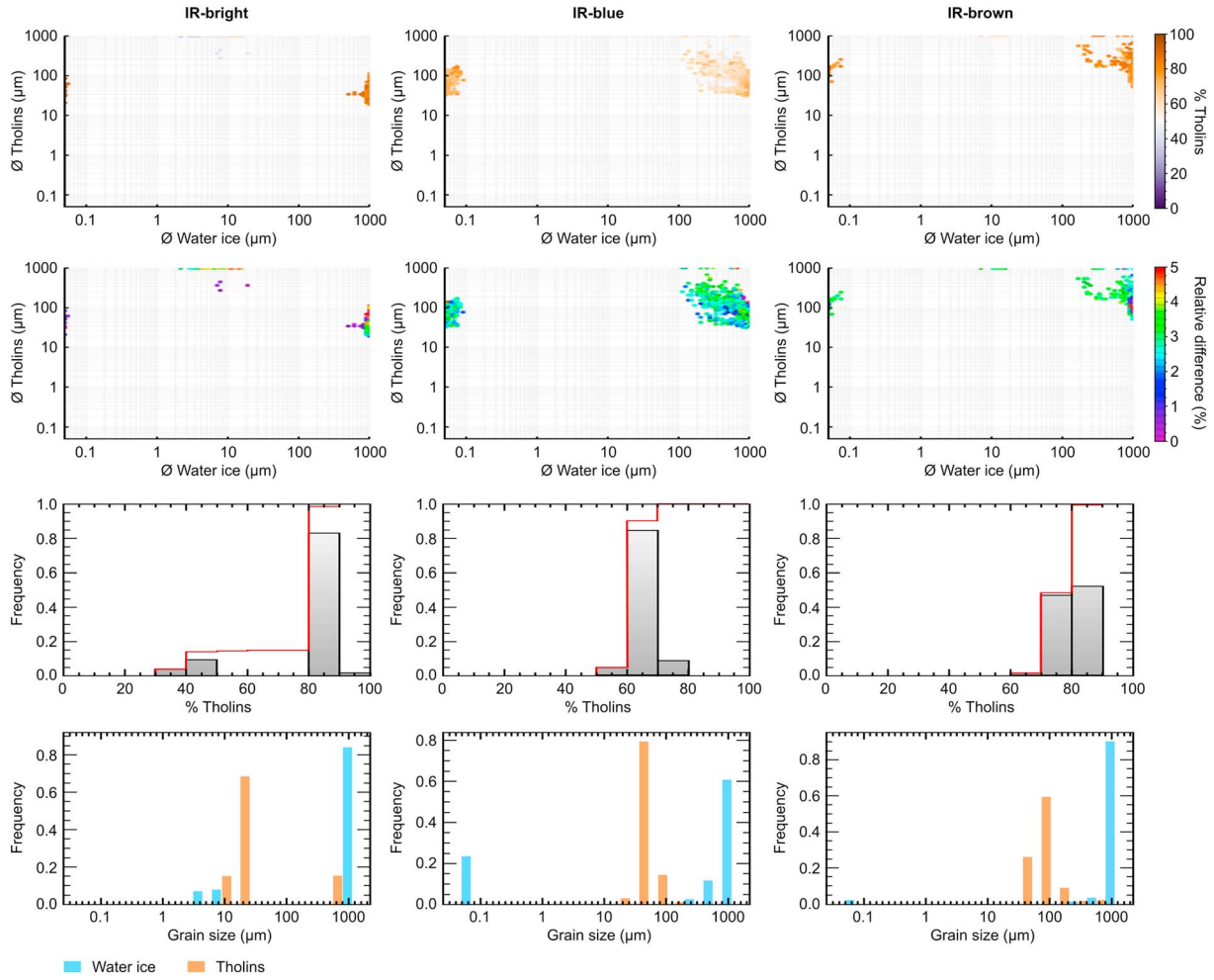

Figure 8. The first row shows diagrams reporting all possible linear mixtures of water ice and tholins that could reproduce the combined single-scattering albedo (ω_0) in each of the 1.27-, 1.57-, and 2.01-µm windows range of the considered IR units by varying grain sizes of both components (diameter in microns) and mixing fraction (% of tholins), for the IR-bright blue and IR-brown units (from left to right column). The second row shows diagrams reporting the relative difference between the observed values (retrieved from the radiative transfer inversion) and the synthetic spectra of linear mixtures. The last two rows are histograms displaying the number of solution for each parameter: (third row) tholins content and (fourth row) water ice and tholins grain sizes (in blue and orange, respectively). Grain sizes are comprised between 50 nm to 1 mm in diameter for both components.

Finally, our mixing model successfully reproduces most of the spectra we selected in the IR-brown units. Following the results of our modeling, the IR-brown dune areas display similar characteristics to those of the IR-blue unit in terms of grain sizes, except that the tholins are expected to be slightly larger (~100 µm in average in Figure 8, right column). However, the distribution in water ice content of the mixture peaks at a higher fraction of tholins, around 80%, like in the IR-bright unit. This validates the initially thought enrichment in water ice for the IR-blue unit relative to the IR-brown unit and its depletion in the dune areas (Rodriguez et al., 2014; Soderblom et al., 2007).

Table 3
Synthesis of the Spectral Mixing Modeling

	IR-bright	IR-blue	IR-brown
Total number of pixels in RoIs	4,585	4,717	1,274
Total number of solutions	4,544	4,717	1,261
Percentage of solutions	99.1	100	98.9
Mixing ratio distribution (in % tholins)	80	60	70–90
Water ice grain size distribution (in µm)	800	600–800	800
Tholin grain size distribution (in µm)	10–25	25–100	50–200

Note. Best retrieved solutions (with the highest frequency) obtained for the IR-bright, IR-blue, and IR-brown spectral units selected within the RoIs (see also Figure 8). RoIs = regions of interest.

5. Geological Interpretations of the Transition Zones Between Infrared Units

5.1. IR-Bright Units

Our spectral mixing model reveals a small amount of water ice (<20%) in the IR-bright units investigated (Figure 8 left column).

Moreover, our modeling indicates that the IR-bright unit is dominated by small-sized (a few tens of microns) tholins expected to result from the atmospheric fallout (Tomasko et al., 2008). This continuous fallout may form a fresh, fine-grained organic sedimentary layer that ends up covering the icebed over geological timescales. Cassini's RADAR can be used either as a SAR imaging sensor (active mode) or as a thermal radiometer (passive mode) at 2.18-cm wavelength (Elachi et al., 2004). Thus, based on these two RADAR modes, Janssen et al. (2016) suggest the presence of water ice in the near surface where ground features display high SAR backscatter and low thermal emissivity at 2.18-cm wavelength. These latter correspond to mountainous terrains and craters (particularly ejecta, rim, and central peak), and they represent only a minor fraction of the whole IR-bright unit. Conversely, it appears that the major fraction of the IR-bright unit on Titan, corresponding to the plains, exhibits a moderate-to-low SAR backscatter and high brightness temperatures, as shown by radiometry data analysis, which is consistent with organic material (Janssen et al., 2016; Lopes et al., 2016; Malaska, Lopes, Williams, et al., 2016). Hence, it has been assumed that the mountainous terrains and craters are partly or entirely coated by a superficial layer of organic sediments (Barnes, Brown, et al., 2007; Clark et al., 2010; Soderblom et al., 2007). As VIMS is only sensitive to the first few microns of Titan's surface, this layer is expected to be sufficiently thick in order to mask the infrared spectral signature of most of the underlying icebed.

Nevertheless, a few patches of IR-blue materials are seen within large IR-bright units (notably Xanadu province) that also show a bluish appearance in VIMS composites (Figure 6). At a global scale, which implies resolutions over a few to several tens of kilometers, the IR-bright units appear spectrally uniform. However, these seemingly uniform IR-bright units exhibit substantial albedo heterogeneities at a smaller scale when the spatial sampling of the images becomes sufficiently high, below 10 km/pixel. Langhans et al. (2012) demonstrated that these IR-bluish heterogeneities possess the spectral behavior of a mixture of IR-bright and IR-blue units. This suggested that those IR-bluish patches are embedded into the IR-bright units and are probably too small to be fully resolved by Cassini's infrared imaging data as part of the IR-blue unit. The IR-bluish patches are found in small SAR-bright mountainous terrains and surrounded by IR-bright and SAR-dark plains (Barnes, Radebaugh, et al., 2007; Soderblom et al., 2007). These features could represent icy outcrops in heavily degraded terrains, as the icebed is washed clean of surficial organic sediments after episodic rainfalls. Alternatively, they could also represent accumulated water ice erosional products coming from the degradation of the icebed and covering an organic layer.

Furthermore, the minor fraction of the IR-bright units represented by mountainous terrains and craters seems to be significantly modified by erosional processes, with sharp incisions by liquid hydrocarbon flows after rainfalls (e.g., Langhans et al., 2012), more than any other terrains on Titan. Fluvial networks cutting through the IR-bright units were first seen in the DISR images acquired during the descent of the Huygens probe in January 2005 (Tomasko et al., 2005). Since then, it has been shown that fluvial features are mostly found in the IR-bright units on Titan (Burr et al., 2009, 2013; Langhans et al., 2012, 2013; Lorenz et al., 2008; Radebaugh et al., 2011). Nevertheless, the selected areas in this study do not seem to be completely covered by channels. Indeed, it has been shown that fluvial features are mainly concentrated to the poles, while only a few occurrences are seen at lower latitudes (Birch, Hayes, Howard, et al., 2016; Lopes et al., 2016; Malaska, Lopes, Williams, et al., 2016). This lack of fluvial features might be a resolution effect, since Cassini's imaging instruments are limited to resolutions at best of 300 m. Few distinct IR-blue channels were identified or merely detected at low latitudes, starting from the IR-bright units and draining into the IR-blue units (Barnes, Radebaugh, et al., 2007; Jaumann et al., 2008, 2010; Langhans et al., 2012; this work). Those channels are commonly bright in SAR swaths. This supports the hypothesis of the IR-bright units being eroded by fluids, from which material detached from the icebed is transported to the IR-blue units (Barnes, Radebaugh, et al., 2007; Jaumann et al., 2008, 2010).

Impact craters are also subject to erosional and transport processes like weathering, mass wasting, fluvial incision, deposition, and even aeolian infilling. Indeed, fluvial and/or aeolian degradation clearly affect crater ejecta, rims, and central peaks and even fill in the crater floors (Neish et al., 2016). This process could explain the presence of materials in the crater floors that are distinct to those detected at the wall, rims, and ejecta of the craters, such as IR-blue materials within Sinlap and IR-brown dune materials within Paxsi, whereas the ejecta, rims, and central peaks, when present, are IR-bright and show marks of incision at some places (Figure 6).

5.2. IR-Blue Units

5.2.1. The Case of Outwash Plains

Apart from the previously mentioned small-scale IR-bluish features embedded in IR-bright areas, IR-blue terrains are mostly found at the margins of IR-bright units and around impact craters. It has been thought that those IR-blue units might host surface material enriched in water ice (Barnes, Radebaugh, et al., 2007; Jaumann et al., 2008, 2010; Le Mouélic et al., 2008; Rodriguez et al., 2006, 2014). Our work (Figure 8 middle column) shows that the spectral signature of the IR-blue units is, indeed, in very good agreement with the water ice enrichment hypothesis relative to the other IR units. The enrichment is particularly striking when comparing the water ice mixing fractions of the nearby IR-bright unit. Indeed, the latter barely exceeds 20% of water ice, whereas the IR-blue unit presents mixing fractions starting from 20% and reaching 50% of water ice. This water ice could correspond to icebed exposure or even icy debris laying on surface after degradation of the icebed. It is also worth noting that, despite a clear enrichment in water ice, IR-blue units are not systematically predominantly made of water ice. As for IR-bright units, the grain size distribution of the water ice component for the IR-blue unit shows grains that are in majority larger than hundreds of microns, but the spread is skewed toward smaller sizes, with the modeling suggesting some submicronic grains (Figure 8 middle column). This heterogeneity in grain sizes could be related to mechanical erosion from material being transported downstream from the IR-bright unit that may break large pebbles of the icebed and then turned them into smaller blocks during transport and deposition onto the IR-blue unit (Barnes, Radebaugh, et al., 2007; Jaumann et al., 2008, 2010). For instance, water ice within IR-blue units located east of Xanadu, as well as those present in Chusuk and Giedi Planitiae, and around the craters, may represent erosion products derived from the fluvial incision of the icebed in the nearby IR-bright units (Figure 6). This water ice could have been washed out and carried by flows of liquid hydrocarbons from presumably more elevated IR-bright units and hence contribute to the slight areal water ice enrichment of the IR-blue units detected by VIMS. The tholin component inferred from our calculations also displays a spread in the grain size distribution, but skewed toward larger sizes, allowing tholins ranging from several tens to hundreds of microns in the IR-blue units, larger than those fit by the model in the IR-bright units. This change in the tholin grain size distribution could argue for a progressive processing, which results in grain size sorting of the organic material from small-sized tholins (analogous to atmospheric aerosols) to larger grains. They may grow in size by compaction or sintering (Barnes et al., 2015) in the depositional layer of the IR-bright units and then be eroded, along with the icebed material, and transported by flows from the IR-bright highlands to the IR-blue areas and deposited there. Thus, these IR-blue units could be the signature of outwash plains hosting icy blocks and pebbles, along with sediment down in size to hundreds of microns. Interestingly, similar materials were detected at the Huygens landing site (Tomasko et al., 2005), an area also located in the IR-blue units, where pebbles are suspected to be made of water ice and overlaid at some places with a layer of darker, finer-grained tholin-like sediments. Both components are being transported from the IR-bright to the IR-blue units through fluvial processes.

Note that the IR-blue units surrounding impact craters, referred as halos in this paper, were originally interpreted as icy deposit sheets set down from vapor plumes formed during impacts, notably in the case of Sinlap crater (Le Mouélic et al., 2008). Here we consider that such icy sheet deposits should be covered by organic material derived from atmospheric fallout and then could be modified by subsequent erosional processes and aeolian deposition. Indeed, IR-bright crater rims are thought to undergo from erosional processes similar to those occurring in the mountainous terrains (Barnes, Radebaugh, et al., 2007; Jaumann et al., 2008, 2010). Icy materials constituting craters rims and ejecta are therefore washed out by rainfalls and/or winds, along with organic coating materials, toward the surrounding icy sheet deposits at lower elevations. This could contribute to exposing the icebed and to the enrichment of water ice around the craters (i.e., IR-blue halos), as suspected for Elivagar Flumina crossing the ejecta blanket of Menrva crater (Radebaugh et al., 2016) for instance. Moreover, Selk crater (199°W, 7°N) may also be a case example of such phenomena, as it has IR-blue units exposed along the outer flank of the entire rim, extending out to the IR-brown sand sea in which the crater is set (Soderblom et al., 2010).

5.2.2. IR-Blue Unit Burial

Our map (Figure 1d) shows that the IR-blue units cover only 1.5% of Titan's surface (1.3×10^6 km^2); this small fraction could be consistent with IR-blue units encroached upon by the dunes in places where the wind can transport sands. Moreover, IR-blue units are commonly located at the eastern boundaries of IR-bright units,

on the downwind side of topographic obstacles (Charnay et al., 2015; Lucas et al., 2014). Thus, this suggests that IR-blue units are preserved from being covered by wind-blown sands and hence from the current dune migration (Malaska, Lopes, Williams, et al., 2016; Malaska, Lopes, Hayes, et al., 2016). To date, the IR-blue halo around Sinlap is still present, as the crater seems well preserved and likely recent (Lorenz et al., 2007). Conversely, for older craters, like Paxsi, the associated icy halos are partly or even fully overtaken by dunes, as seen in the SAR swaths. Thus, we infer that these IR-blue units should exist until the dunes entirely buried them.

5.3. IR-Brown Units

Numerous analyses of VIMS observations have suggested that the VIMS spectrum of dunes does not correspond to water ice but broadly matches with that of solid organics, including analogs of airborne aerosols (tholins; Barnes, Brown, et al., 2007, 2008; Clark et al., 2010; McCord et al., 2006, 2008; Rodriguez et al., 2014; Soderblom et al., 2007). Moreover, measurements performed by the RADAR in passive radiometer mode have confirmed that the composition of the dunes cannot be based on pure water ice (Janssen et al., 2009, 2016). Further studies even potentially identified absorption signatures of benzene (Clark et al., 2010) and acetylene (Singh et al., 2016) in these dune areas. Our spectral mixing model reveals that IR-brown units are predominantly made of tholins (80% in average in Figure 8, right column), with a grain size distribution similar to that of the IR-blue units, ranging from several tens to hundreds of microns. The predominance of organic material in dune areas is in agreement with the results obtained in the aforementioned studies. Regarding the morphological and spectral properties of the three infrared units, it seems reasonable to think that at least a part of the dune material originate from the IR-bright areas selected in our study. Strong arguments supporting this hypothesis come from the combined altitude, geographic, and compositional relationships between these units. Indeed, rough estimation of Titan's relative altitude of the three infrared units seems to point to IR-bright unit above the IR-brown and IR-blue being at intermediate altitude (e.g., Radebaugh et al., 2016). Furthermore, in each of the regions studied we observe a geographic connection between IR-bright, IR-blue, and IR-brown units, systematically in that order. Finally, derived spectral properties of the three units lead to the estimation of the evaluation of their surface composition and granulometry, all units being dominated by organics and the grain size distribution of organics shifting toward larger sizes from IR-bright to IR-brown units and that of water ice being relatively equivalent from a unit to another (Table 3). Putting together these arguments, we can fairly suggest that organic materials detected in IR-bright units derived from atmospheric fallout could be modified by surficial processes and end up in sand seas to compose the dunes. The smallest grains of tholins (tens of microns) may be representative of a coating of organic dust, covering the dune material made of organic sand that is expected to consist of larger particles, exceeding hundreds of microns (over 200 μm in Burr et al., 2015; Lorenz, 2014). This coating could mask part of the dune material at infrared wavelengths, which are only sensitive to the very first microns of the surface. Such organic dust has been detected by the DISR instrument at the Huygens landing site (Schröder et al., 2012), revealing the widespread geographic distribution of dust on Titan, especially over IR-blue and IR-brown units. Having a similar size distribution to that in the IR-blue units, this organic dust can originate from part of the IR-blue outwash plains, being then blown by the wind and accumulating in the IR-brown areas. The larger sand material composing the dunes may possibly be formed from this organic dust, itself formed from atmospheric aerosols. Finally, the large-grained water ice component of the IR-brown dune areas of our study may represent the partial areal exposure of the icebed in some of the interdunes in areas of more limited organic sediment availability, as already suspected by Barnes et al. (2008), Rodriguez et al. (2014), and Bonnefoy et al. (2016).

5.4. Connecting the Infrared Units

If the organic sand forming the dunes derives from the atmospheric fallout, then the composition of the dune material and its source should directly reflect that of the haze particles. Nonetheless, despite the fact that dunes are commonly found in the IR-brown units (Rodriguez et al., 2014; Soderblom et al., 2007), the complete history of organic sand, from its source to its sinking, still remains enigmatic. Here we propose that the sources of the dune materials could either (1) show the same spectral signature as the dunes and hence appear also IR-brown (same composition and grain size according to our spectral mixing model) or (2) have a different spectral signature and might appear IR-bright (same composition but different grain size) due to mechanical erosion and transport processes affecting both the icebed and the organic materials masking it.

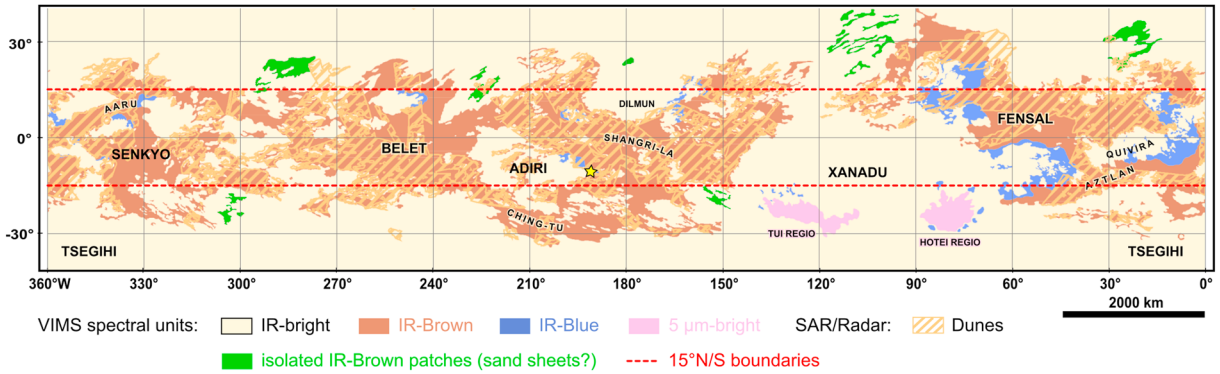

Figure 9. Same as Figure 1d, where the green areas represent isolated IR-brown patches that could correspond to potential sand sheets. Red lines mark the 15°N/S boundaries. Note that most of those candidate areas are not observed in SAR imaging mode (see Figure 1c). VIMS = Visual and Infrared Mapping Spectrometer; SAR = Synthetic Aperture Radar.

In order to test the first hypothesis, it is necessary to look for IR-brown areas where SAR imaging does not detect any dunes. A few isolated IR-brown dune-free areas are seen at the midlatitudes, around 30° latitudes (green areas in Figure 9) and could be potential sources for dune material, but most of them are not seen in SAR images. However, the sizes and locations of these possible sand sheets can hardly make those areas the sources of the equatorial dunes. Their locations are particularly difficult to reconcile with the equatorial concentration of the dunes, since the sediment pathways are commonly expected to diverge poleward at latitudes higher than 15°N/S (Charnay et al., 2015; Lucas et al., 2014; Malaska, Lopes, Hayes, et al., 2016). If these potential sand sheets can be possibly connected to the few isolated dunes found at higher latitudes, they cannot explain the presence of most of the large sand seas found closer to the equator. Following the predictions of Lucas et al. (2014) and Charnay et al. (2015), the sand fluxes converge toward the equator only for latitudes between 15°N/S, where most of the dunes are observed, making this latitudinal belt a sand trap. Interestingly, Malaska, Lopes, Hayes, et al. (2016) have shown that the transport of dune material found within about 15°N/S is stable and remains along the equator. Otherwise, outside these boundaries, the dune material tends to deviate poleward and to accumulate in the midlatitudes, around 30° latitudes (Malaska, Lopes, Hayes, et al., 2016). Hence, the sand material detected in the IR-brown dunes areas should originate from the equatorial regions.

Hence, we propose an alternative explanation, where the sources of dune material have a different spectral signature corresponding to that of the IR-bright unit. In this case, sand material could derive from the degradation of the high-standing landforms in the IR-bright units and the subsequent transport to the lowlands, which consist of the IR-blue and IR-brown units. To illustrate this assumption, we propose a cartoon model (Figure 10) showing a complete history of the sediment transport in the equatorial regions, by combining atmospheric and surficial processes. On highlands, methane rainfalls cause the fluvial erosion of the icebed and the organic sedimentary layer masking it. This organic sedimentary layer being primarily made of the smallest tholins grains (Figure 8 left column), accumulated from atmospheric fallout, creates the IR-bright unit that exhibits a high albedo in VIMS spectra with respect to the other considered units. Erosion products, comprising both water ice and organic coating materials, are transported through channels flowing across the IR-bright plains toward lowlands. Depending on the outflow in the channels, large particles to pebbles could be transported by the liquids (Collins, 2005). Then, the deposition of these erosion products results in grain size sorting and hence implies a compositional discrimination where ice-rich, large-grained materials lie on top and creates the IR-blue unit (outwash plains or alluvial fans in Birch, Hayes, Dietrich, et al., 2016; Radebaugh et al., 2016). In IR-blue outwash plains, materials are blown farther away by the winds, causing further grain size sorting, where aeolian processes may create granular mixtures of water ice and organic materials. These granular mixtures become the IR-brown unit, in which the grains that are small enough to saltate (sand) are shaped into dunes and the grains even smaller are blown away into dust storms.

As explained earlier, some traces of large-grained water ice are expected by our spectral mixing model, which could be compatible with the presence of the water ice exposed in the interdunes (icebed or icy debris) that

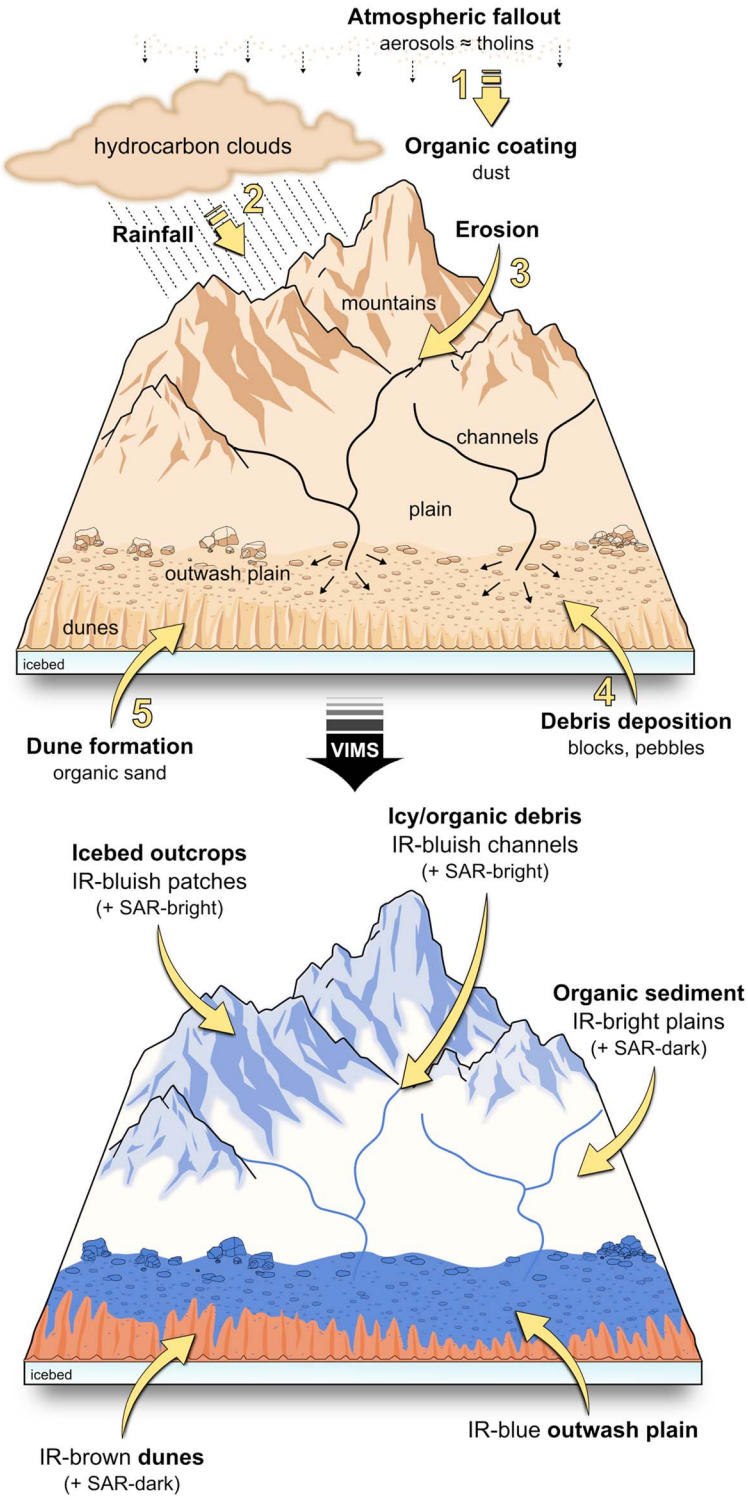

Figure 10. (top) Cartoon model illustrating the series of processes that could explain the actual distribution and the structural relationship of the infrared units in the equatorial belt of Titan, as seen through usual VIMS composites (bottom). In the atmosphere, photochemically produced aerosols fall down on the surface and form an organic sedimentary layer covering the icebed. Additionally, methane condenses and precipitates, which leads to the degradation of mountainous terrains (and craters rims) via rainfalls. This degradation is followed by the transport of debris, including organic sediment and icebed material, through fluvial channels crossing the plains (and ejecta blankets). The debris are then washed out at the margins of the IR-bright units, resulting in a IR-blue outwash plain exhibiting blocks and pebbles similar to those seen in the Huygens landing site (Tomasko et al., 2005), which is also IR-blue (Rodriguez et al., 2006). The outer boundary of the IR-blue units marks the beginning of the dune fields formation, essentially made of organic sand. IR-bluish patches seen in mountainous terrains indicate a strong erosion of those terrains that could probably expose the icebed. VIMS = Visual and Infrared Mapping Spectrometer; SAR = Synthetic Aperture Radar.

are included alongside with dunes in the IR-brown unit in our study. The interdune composition and/or grain size is seen to vary spatially over Titan (Bonnefoy et al., 2016; Le Gall et al., 2011, 2012; Lucas et al., 2017) and could correspond to that of the neighboring terrains that the dunes are developing upon, such as mountainous terrains, crater ejecta and rims, or even IR-blue units. Thus, the interdune signature in the infrared range strongly depends on the location of the investigated dune areas and the spatial resolution of the available VIMS cubes. We suggest that the dunes are actively developing from the fine organic material transported along with icy grains over the older water ice-rich hills and plains. Recent analysis of the morphometric variations of the dunes with Cassini/RADAR observations tends to confirm those assumptions, as described in Bishop et al. (2017) and Lewis et al. (2017). Dunes are expected to be wider at low latitudes, which generally corresponds to the sand seas centers (Le Gall et al., 2011; Savage et al., 2014). Conversely, they are narrower at the margins or near topographic obstacles (Le Gall et al., 2012), which could explain the exposure of underlying ice material in the sand-free interdunes.

6. Conclusions and Perspectives

We studied the infrared properties and geological relationships of the IR-bright, IR-blue, and IR-brown units detected in the equatorial regions of Titan based on Cassini/VIMS data and Cassini/RADAR SAR imager for detailing the geomorphological context. Thanks to the joint use of a radiative transfer and spectral mixing models for grains of water ice and tholins, we provided new constraints about the composition and structural relationships between the three main IR units found in the Titan's equatorial belt. Our results support a number of assumptions made in previous studies. All the IR units considered appear to contain be dominated by organics (here tholins) that likely derive from the atmospheric fallout. The presence of a mixture of medium-sized tholins and large grained water ice could explain the low albedo of IR-brown and IR-blue units relative to the IR-bright unit, composed in majority by fine-grained tholins. Interestingly, IR-blue units are clearly enriched in large water ice grains in comparison to the other considered units. This water ice material could result from the mechanical erosion of the icebed following hydrocarbon rainfalls on highlands. Thus, we can confidently suggest a scenario that could explain the current distribution of the IR units present in the equatorial regions, as shown in Figure 10. This distribution is very similar to that of transition areas from mountains to stony and sandy deserts on Earth (regs and ergs, respectively). We therefore expect the presence of mountainous terrains near the IR-blue and IR-brown dunes transition. IR-blue units would be analogous to the terrestrial stony deserts, where ice and organic materials are laid after erosional and depositional processes from the IR-bright units. Conversely, IR-brown units would be analogous to the terrestrial sandy deserts that are covered by longitudinal dunes mainly made of organic sand, in the case of Titan.

Since we propose geological processes that are partly driven by the topography, as the IR-bright mountainous terrains and craters (ejecta, rim, and central peak) must be elevated relative to the IR-blue outwash plains and IR-brown dunes areas, the topographic distribution of the three IR units should thoroughly be investigated. Analysis of topographic data acquired by the Cassini/RADAR instrument could support our assumptions, particularly with the SARTopo (Stiles et al., 2009) and Altimetry (Zebker et al., 2009) data sets. Indeed, by using these data sets, recent studies obtained significant information about the superposition relations between the major landscapes seen on Titan. Mountainous terrains and craters are often defined as the oldest geomorphologic units and are found to be topographically higher than plains and dunes (Birch, Hayes, Howard, et al., 2016; Lopes et al., 2016; Malaska, Lopes, Williams, et al., 2016). However, the horizontal resolution and vertical accuracy of those data are not necessarily suited for the relatively small scale of the transition zones studied here. For instance, an elevation difference of a few tens of meters will be comprised within the vertical accuracy of the topographic data (75 m for SARTopo and 35–50 m for Altimetry). Despite uncertainties on Titan's topography, a recent study of Menrva crater region shows a topographic profile (Figure 10 from Radebaugh et al., 2016), which describe a moderate regional gradient from the elevated crater rim to the end of the Elivagar Flumina fans, in the lowlands. This latter work exactly matches with our proposed scenario illustrated in Figure 10. Additionally, an accurate and complete model for sediment formation and transport could test our hypotheses, providing further constraints in the origin and transport of debris through liquid hydrocarbons and/or winds, from the highs (IR-bright unit) to the outwash plains (IR-blue unit) and sand seas (IR-brown unit).

Acknowledgments

We gratefully thank the work done by Cassini/VIMS team that made our spectral analysis possible. We also thank the Cassini/RADAR team for providing the RADAR SAR database utilized in this paper. The Cassini ISS, VIMS, and RADAR data are made publicly available through the NASA Planetary Data System Imaging Node portal (http://pds-imaging.jpl.nasa.gov/portal). This work has been carried out at the DLR Institute of Planetary Research and is also partly supported by the Institut Universitaire de France. We also acknowledge financial support from the UnivEarthS LabEx program of Sorbonne Paris Cite (ANR-10-LABX-0023 and ANR-11-IDEX-0005-02) and the French National Research Agency (ANR-APOSTIC-11-BS56-002 and ANR-12-BS05-001-3/EXO-DUNES). T. C. was funded by the CNES Research Fellowship Program in Space Sciences. We wish to thank Jason M. Soderblom and an anonymous referee for the very thorough and constructive review that significantly improved the manuscript.

References

Barnes, J. W., Bow, J., Schwartz, J., Brown, R. H., Soderblom, J. M., Hayes, A. G., et al. (2011). Organic sedimentary deposits in Titan's dry lakebeds: Probable evaporite. *Icarus*, *216*(1), 136–140. https://doi.org/10.1016/j.icarus.2011.08.022

Barnes, J. W., Brown, R. H., Soderblom, J. M., Soderblom, L. A., Jaumann, R., Jackson, B., et al. (2009). Shoreline features of Titan's Ontario Lacus from Cassini/VIMS observations. *Icarus*, *201*(1), 217–225. https://doi.org/10.1016/j.icarus.2008.12.028

Barnes, J. W., Brown, R. H., Soderblom, L., Buratti, B. J., Sotin, C., Rodriguez, S., et al. (2007). Global-scale surface spectral variations on Titan seen from Cassini/VIMS. *Icarus*, *186*(1), 242–258. https://doi.org/10.1016/j.icarus.2006.08.021

Barnes, J. W., Brown, R. H., Soderblom, L., Sotin, C., Le Mouélic, S., Rodriguez, S., et al. (2008). Spectroscopy, morphometry, and photoclinometry of Titan's dunefields from Cassini/VIMS. *Icarus*, *195*(1), 400–414. https://doi.org/10.1016/j.icarus.2007.12.006

Barnes, J. W., Lorenz, R. D., Radebaugh, J., Hayes, A. G., Arnold, K., & Chandler, C. (2015). Production and global transport of Titan's sand particles. *Planetary Science*, *4*(1), 1–19. https://doi.org/10.1186/s13535-015-0004-y

Barnes, J. W., Radebaugh, J., Brown, R. H., Wall, S., Soderblom, L., Lunine, J., et al. (2007). Near-infrared spectral mapping of Titan's mountains and channels. *Journal of Geophysical Research*, *112*, E11006. https://doi.org/10.1029/2007JE002932

Birch, S. P. D., Hayes, A. G., Dietrich, W. E., Howard, A. D., Bristow, C. S., Malaska, M. J., et al. (2016). Geomorphologic mapping of Titan's polar terrains: Constraining surface processes and landscape evolution. *Icarus*, *282*, 214–236. https://doi.org/10.1016/j.icarus.2016.08.003

Birch, S. P. D., Hayes, A. G., Howard, A. D., Moore, J. M., & Radebaugh, J. (2016). Alluvial fan morphology, distribution and formation on Titan. *Icarus*, *270*, 238–247. https://doi.org/10.1016/j.icarus.2016.02.013

Bishop, B., Lewis, R. C., Radebaugh, J., & Christiansen, E. H. (2017). Spatial variations of dune parameters and relationship to elevation and geographic position within the Belet sand sea. In the 48th Lunar and Planetary Science Conference Abstracts.

Bonnefoy, L. E., Hayes, A. G., Hayne, P. O., Malaska, M. J., Le Gall, A., Solomonidou, A., & Lucas, A. (2016). Compositional and spatial variations in Titan dune and interdune regions from Cassini {VIMS} and {RADAR}. *Icarus*, *270*, 222–237. https://doi.org/10.1016/j.icarus.2015.09.014

Brassé, C., Muñoz, O., Coll, P., & Raulin, F. (2015). Optical constants of Titan aerosols and their tholins analogs: Experimental results and modeling/observational data. *Planetary and Space Science*, *109-110*, 159–174. https://doi.org/10.1016/j.pss.2015.02.012

Brown, R. H., Baines, K. H., Bellucci, G., Bibring, J. P., Buratti, B. J., Capaccioni, F., et al. (2004). The Cassini visual and infrared mapping spectrometer (VIMS) investigation. In C. Russell (Ed.), *The Cassini-Huygens mission* (pp. 111–168). Netherlands: Springer. https://doi.org/10.1007/1-4020-3874-7_3

Buratti, B. J., Sotin, C., Lawrence, K., Brown, R. H., Le Mouélic, S., Soderblom, J. M., et al. (2012). A newly discovered impact crater in Titan's Senkyo: Cassini VIMS observations and comparison with other impact features. *Planetary and Space Science*, *60*(1), 18–25. https://doi.org/10.1016/j.pss.2011.05.004

Burr, D. M., Bridges, N. T., Marshall, J. R., Smith, J. K., White, B. R., & Emery, J. P. (2015). Higher-than-predicted saltation threshold wind speeds on titan. *Nature*, *517*(7532), 60–63. https://doi.org/10.1038/nature14088

Burr, D. M., Drummond, S. A., Cartwright, R., Black, B. A., & Perron, J. T. (2013). Morphology of fluvial networks on Titan: Evidence for structural control. *Icarus*, *226*(1), 742–759. https://doi.org/10.1016/j.icarus.2013.06.016

Burr, D. M., Jacobsen, R. E., Roth, D. L., Phillips, C. B., Mitchell, K. L., & Viola, D. (2009). Fluvial network analysis on Titan: Evidence for subsurface structures and west-to-east wind flow, southwestern Xanadu. *Geophysical Research Letters*, *36*, L22203. https://doi.org/10.1029/2009GL040909

Cable, M. L., Horst, S. M., Hodyss, R., Beauchamp, P. M., Smith, M. A., & Willis, P. A. (2012). Titan tholins: Simulating Titan organic chemistry in the Cassini-Huygens era. *Chemical Reviews*, *112*(3), 1882–1909. https://doi.org/10.1021/cr200221x

Charnay, B., Barth, E., Rafkin, S., Narteau, C., Lebonnois, S., Rodriguez, S., et al. (2015). Methane storms as a driver of Titan's dune orientation. *Nature*, *8*(5), 362–366. https://doi.org/10.1038/ngeo2406

Clark, R. N., Curchin, J. M., Barnes, J. W., Jaumann, R., Soderblom, L., Cruikshank, D. P., et al. (2010). Detection and mapping of hydrocarbon deposits on Titan. *Journal of Geophysical Research*, *115*, E10005. https://doi.org/10.1029/2009JE003369

Collins, G. C. (2005). Relative rates of fluvial bedrock incision on Titan and Earth. *Geophysical Research Letters*, *32*, L22202. https://doi.org/10.1029/2005GL024551

Combes, M., Vapillon, L., Gendron, E., Coustenis, A., Lai, O., Wittemberg, R., & Sirdey, R. (1997). Spatially resolved images of Titan by means of adaptive optics. *Icarus*, *129*(2), 482–497. https://doi.org/10.1006/icar.1997.5772

Cornet, T., Bourgeois, O., Le Mouélic, S., Rodriguez, S., Lopez Gonzalez, T., Sotin, C., et al. (2012). Geomorphological significance of Ontario Lacus on Titan: Integrated interpretation of Cassini VIMS, ISS and RADAR data and comparison with the Etosha Pan (Namibia). *Icarus*, *218*(2), 788–806. https://doi.org/10.1016/j.icarus.2012.01.013

Coustenis, A., Gendron, E., Lai, O., Véran, J. P., Woillez, J., Combes, M., et al. (2001). Images of Titan at 1.3 and 1.6 μm with adaptive optics at the CFHT. *Icarus*, *154*(2), 501–515. https://doi.org/10.1006/icar.2001.6643

Coustenis, A., Hirtzig, M., Gendron, E., Drossart, P., Lai, O., Combes, M., & Negrão, A. (2005). Maps of Titan's surface from 1 to 2.5 μm. *Icarus*, *177*(1), 89–105. https://doi.org/10.1016/j.icarus.2005.03.012

Coustenis, A., Lellouch, E., Maillard, J. P., & McKay, C. P. (1995). Titan's surface: Composition and variability from the near-infrared albedo. *Icarus*, *118*(1), 87–104. https://doi.org/10.1006/icar.1995.1179

de Kok, R., Irwin, P. G. J., Teanby, N. A., Lellouch, E., Bézard, B., Vinatier, S., et al. (2007). Oxygen compounds in Titan's stratosphere observed by Cassini CIRS. *Icarus*, *186*(2), 354–363. https://doi.org/10.1016/j.icarus.2006.09.016

Elachi, C., Allison, M. D., Borgarelli, L., Encrenaz, P., Im, E., Janssen, M. A., et al. (2004). Radar: The Cassini titan radar mapper. *Space Science Reviews*, *115*(1–4), 71–110. https://doi.org/10.1007/s11214-004-1438-9

Evans, K. F. (2007). SHDOMPPDA: A radiative transfer model for cloudy sky data assimilation. *Journal of the Atmospheric Sciences*, *64*(11), 3854–3864. https://doi.org/10.1175/2006JAS2047.1

Fortes, A. (2012). Titan's internal structure and the evolutionary consequences. *Planetary and Space Science*, *60*(1), 975–978.

Fulchignoni, M., Ferri, F., Angrilli, F., Ball, A. J., Bar-Nun, A., Barucci, M. A., et al. (2005). In-situ measurements of the physical characteristics of Titan's environment. *Nature*, *438*(7069), 785–791. https://doi.org/10.1038/nature04314

Griffith, C. A., Lora, J. M., Turner, J., Penteado, P. F., Brown, R. H., Tomasko, M. G., et al. (2012). Possible tropical lakes on Titan from observations of dark terrain. *Nature*, *486*(7402), 237–239. https://doi.org/10.1038/nature11165

Griffith, C. A., Owen, T., Geballe, T. R., Rayner, J., & Rannou, P. (2003). Evidence for the exposure of water ice on Titan's surface. *Science*, *300*(5619), 628–630. https://doi.org/10.1126/science.1081897

Griffith, C. A., Owen, T., & Wagener, R. (1991). Titan's surface and troposphere, investigated with ground-based near-infrared observations. *Icarus*, *93*(2), 362–378. https://doi.org/10.1016/0019-1035(91)90219-J

Grundy, W. M., & Schmitt, B. (1998). The temperature-dependent near-infrared absorption spectrum of hexagonal H_2O ice. *Journal of Geophysical Research*, *103*(E11), 25,809–25,822. https://doi.org/10.1029/98JE00738

Hapke, B. (2012). *Theory of reflectance and emittance spectroscopy (topics in remote sensing)*, (2nd ed.p. 513). Cambridge: Cambridge University Press. https://doi.org/10.1017/CBO9781139025683

Hirtzig, M., Bézard, B., Lellouch, E., Coustenis, A., de Bergh, C., Drossart, P., et al. (2013). Titan's surface and atmosphere from Cassini/VIMS data with updated methane opacity. *Icarus*, *226*(1), 470–486. https://doi.org/10.1016/j.icarus.2013.05.033

Hirtzig, M., Coustenis, A., Lai, O., Emsellem, E., Pecontal-Rousset, A., Rannou, P., et al. (2005). Near-infrared study of Titan's resolved disk in spectro-imaging with CFHT/OASIS. *Planetary and Space Science*, *53*(5), 535–556. https://doi.org/10.1016/j.pss.2004.08.006

Hofgartner, J. D., Buratti, B. J., Brown, R. H., Barnes, J. W., Sotin, C., & Lawrence, K. (2016). Erosion of Titan's craters from Cassini/RADAR and VIMS imagery. In the 47th Lunar and Planetary Science Conference Abstracts.

Janssen, M. A., Le Gall, A., Lopes, R. M., Lorenz, R. D., Malaska, M. J., Hayes, A. G., et al. (2016). Titan's surface at 2.18-cm wavelength imaged by the Cassini RADAR radiometer: Results and interpretations through the first ten years of observation. *Icarus*, *270*, 443–459. https://doi.org/10.1016/j.icarus.2015.09.027

Janssen, M. A., Lorenz, R. D., West, R., Paganelli, F., Lopes, R. M., Kirk, R. L., et al. (2009). Titan's surface at 2.2-cm wavelength imaged by the Cassini RADAR radiometer: Calibration and first results. *Icarus*, *200*(1), 222–239. https://doi.org/10.1016/j.icarus.2008.10.017

Jaumann, R., Brown, R. H., Stephan, K., Barnes, J. W., Soderblom, L. A., Sotin, C., et al. (2008). Fluvial erosion and post-erosional processes on Titan. *Icarus*, *197*(2), 526–538. https://doi.org/10.1016/j.icarus.2008.06.002

Jaumann, R., Kirk, R. L., Lorenz, R. D., Lopes, R. M. C., Stofan, E., Turtle, E. P., et al. (2010). Geology and surface processes on Titan. In R. H. Brown (Ed.), *Titan from Cassini-Huygens* (pp. 75–140). Netherlands: Springer. https://doi.org/10.1007/978-1-4020-9215-2_5

Khare, B. N., Sagan, C., Arakawa, E. T., Suits, F., Callcott, T. A., & Williams, M. W. (1984). Optical constants of organic tholins produced in a simulated Titanian atmosphere: From soft x-ray to microwave frequencies. *Icarus*, *60*(1), 127–137. https://doi.org/10.1016/0019-1035(84)90142-8

Krasnopolsky, V. A. (2009). A photochemical model of Titan's atmosphere and ionosphere. *Icarus*, *201*(1), 226–256. https://doi.org/10.1016/j.icarus.2008.12.038

Krasnopolsky, V. A. (2014). Chemical composition of Titan's atmosphere and ionosphere: Observations and the photochemical model. *Icarus*, *236*, 83–91. https://doi.org/10.1016/j.icarus.2014.03.041

Langhans, M. H., Jaumann, R., Stephan, K., Brown, R. H., Buratti, B. J., Clark, R. N., et al. (2012). Titan's fluvial valleys: Morphology, distribution, and spectral properties. *Planetary and Space Science*, *60*(1), 34–51. https://doi.org/10.1016/j.pss.2011.01.020

Langhans, M. H., Lunine, J. I., & Mitri, G. (2013). Titan's Xanadu region: Geomorphology and formation scenario. *Icarus*, *223*(2), 796–803. https://doi.org/10.1016/j.icarus.2013.01.016

Lavvas, P. P., Coustenis, A., & Vardavas, I. M. (2008a). Coupling photochemistry with haze formation in Titan's atmosphere. Part I: Model description. *Planetary and Space Science*, *56*(1), 27–66. https://doi.org/10.1016/j.pss.2007.05.026

Lavvas, P. P., Coustenis, A., & Vardavas, I. M. (2008b). Coupling photochemistry with haze formation in Titan's atmosphere. Part II: Results and validation with Cassini/Huygens data. *Planetary and Space Science*, *56*(1), 67–99. https://doi.org/10.1016/j.pss.2007.05.027

Le Gall, A., Hayes, A. G., Ewing, R., Janssen, M. A., Radebaugh, J., Savage, C., et al. (2012). Latitudinal and altitudinal controls of Titan's dune field morphometry. *Icarus*, *217*(1), 231–242. https://doi.org/10.1016/j.icarus.2011.10.024

Le Gall, A., Janssen, M. A., Wye, L. C., Hayes, A. G., Radebaugh, J., Savage, C., et al. (2011). Cassini SAR, radiometry, scatterometry and altimetry observations of Titan's dune fields. *Icarus*, *213*(2), 608–624. https://doi.org/10.1016/j.icarus.2011.03.026

Le Mouélic, S., Cornet, T., Rodriguez, S., Sotin, C., Barnes, J. W., Brown, R. H., et al. (2016). Producing seamless global mosaics of Titan with the VIMS imaging spectrometer. In the 47th Lunar and Planetary Science Conference Abstracts.

Le Mouélic, S., Cornet, T., Rodriguez, S., Sotin, C., Barnes, J. W., Baines, K. H., et al. (2012). Global mapping of Titan's surface using an empirical processing method for the atmospheric and photometric correction of Cassini/VIMS images. *Planetary and Space Science*, *73*(1), 178–190. https://doi.org/10.1016/j.pss.2012.09.008

Le Mouélic, S., Paillou, P., Janssen, M. A., Barnes, J. W., Rodriguez, S., Sotin, C., et al. (2008). Mapping and interpretation of Sinlap crater on Titan using Cassini VIMS and RADAR data. *Journal of Geophysical Research*, *113*, E04003. https://doi.org/10.1029/2007JE002965

Lewis, R. C., Bishop, B., Radebaugh, J., & Christiansen, E. H. (2017). A comparative analysis of sediment transport and deposition trends of the sand sea of Earth and Titan. In the 48th Lunar and Planetary Science Conference Abstracts.

Lopes, R. M. C., Malaska, M. J., Solomonidou, A., Le Gall, A., Janssen, M. A., Neish, C. D., et al. (2016). Nature, distribution, and origin of Titan's undifferentiated plains. *Icarus*, *270*, 162–182. https://doi.org/10.1016/j.icarus.2015.11.034

Lopes, R. M. C., Stofan, E. R., Peckyno, R., Radebaugh, J., Mitchell, K. L., Mitri, G., et al. (2010). Distribution and interplay of geologic processes on Titan from Cassini radar data. *Icarus*, *205*(2), 540–558. https://doi.org/10.1016/j.icarus.2009.08.010

Lorenz, R. D. (2014). Physics of saltation and sand transport on Titan. A brief review. *Icarus*, *230*, 162–167. https://doi.org/10.1016/j.icarus.2013.06.023

Lorenz, R. D., Lopes, R. M., Paganelli, F., Lunine, J. I., Kirk, R. L., Mitchell, K. L., et al. (2008). Fluvial channels on Titan: Initial Cassini RADAR observations. *Planetary and Space Science*, *56*(8), 1132–1144. https://doi.org/10.1016/j.pss.2008.02.009

Lorenz, R. D., Wood, C. A., Lunine, J. I., Wall, S. D., Lopes, R. M., Mitchell, K. L., et al. (2007). Titan's young surface: Initial impact crater survey by Cassini RADAR and model comparison. *Geophysical Research Letters*, *34*, L07204. https://doi.org/10.1029/2006GL028971

Lucas, A., Rodriguez, S., Lemonnier, F., Le Gall, A., Ferrari, C., Paillou, P., & Narteau, C. (2017). Texture and composition of Titan's equatorial region inferred from Cassini SAR inversion: Implications for aeolian transport at Saturn's largest moon. ArXiv e-prints.

Lucas, A., Rodriguez, S., Narteau, C., Charnay, B., du Pont, S. C., Tokano, T., et al. (2014). Growth mechanisms and dune orientation on Titan. *Geophysical Research Letters*, *41*, 6093–6100. https://doi.org/10.1002/2014GL060971

MacKenzie, S. M., & Barnes, J. W. (2016). Compositional similarities and distinctions between Titan's evaporitic terrains. *The Astrophysical Journal*, *821*(1). https://doi.org/10.3847/0004-637X/821/1/17

MacKenzie, S. M., Barnes, J. W., Sotin, C., Soderblom, J. M., Le Mouélic, S., Rodriguez, S., et al. (2014). Evidence of Titan's climate history from evaporite distribution. *Icarus*, *243*, 191–207. https://doi.org/10.1016/j.icarus.2014.08.022

Malaska, M. J., Lopes, R. M., Hayes, A. G., Radebaugh, J., Lorenz, R. D., & Turtle, E. P. (2016). Material transport map of Titan: The fate of dunes. *Icarus*, *270*, 183–196. https://doi.org/10.1016/j.icarus.2015.09.029

Malaska, M. J., Lopes, R. M. C., Williams, D. A., Neish, C. D., Solomonidou, A., Soderblom, J. M., et al. (2016). Geomorphological map of Afekan Crater region, Titan: Terrain relationships in the equatorial and mid-latitude regions. *Icarus*, *270*, 130–161. https://doi.org/10.1016/j.icarus.2016.02.021

Maltagliati, L., Rodriguez, S., Sotin, C., Cornet, T., Rannou, P., Le Mouélic, S., et al. (2015). Simultaneous mapping of Titan's surface albedo and aerosol opacity from Cassini/VIMS massive inversion. In the 10th European Planetary Science Congress.

McCord, T. B., Hansen, G. B., Buratti, B. J., Clark, R. N., Cruikshank, D. P., D'Aversa, E., et al. (2006). Composition of Titan's surface from Cassini VIMS. *Planetary and Space Science*, *54*(15), 1524–1539. https://doi.org/10.1016/j.pss.2006.06.007

McCord, T. B., Hayne, P., Combe, J. P., Hansen, G. B., Barnes, J. W., Rodriguez, S., et al. (2008). Titan's surface: Search for spectral diversity and composition using the Cassini VIMS investigation. *Icarus*, *194*(1), 212–242. https://doi.org/10.1016/j.icarus.2007.08.039

Mustard, J. F., & Sunshine, J. M. (1999). Spectral analysis for Earth science: Investigation using remote sensing data. In A. M. Rencz (Ed.), *Remote sensing for Earth sciences: Manual of remote sensing* (3rd ed., Vol. 3, pp. 251–306). New York: John Wiley.

Negrão, A., Coustenis, A., Lellouch, E., Maillard, J. P., Rannou, P., Schmitt, B., et al. (2006). Titan's surface albedo variations over a Titan season from near-infrared CFHT/FTS spectra. *Planetary and Space Science*, *54*(12), 1225–1246. https://doi.org/10.1016/j.pss.2006.05.031

Neish, C. D., Barnes, J. W., Sotin, C., MacKenzie, S., Soderblom, J. M., Le Mouélic, S., et al. (2015). Spectral properties of Titan's impact craters imply chemical weathering of its surface. *Geophysical Research Letters*, *42*, 3746–3754. https://doi.org/10.1002/2015GL063824

Neish, C. D., Molaro, J. L., Lora, J. M., Howard, A. D., Kirk, R. L., Schenk, P., et al. (2016). Fluvial erosion as a mechanism for crater modification on Titan. *Icarus*, *270*, 114–129. https://doi.org/10.1016/j.icarus.2015.07.022

Niemann, H. B., Atreya, S. K., Demick, J. E., Gautier, D., Haberman, J. A., Harpold, D. N., et al. (2010). Composition of Titan's lower atmosphere and simple surface volatiles as measured by the Cassini-Huygens probe gas chromatograph mass spectrometer experiment. *Journal of Geophysical Research*, *115*, E12006. https://doi.org/10.1029/2010JE003659

Radebaugh, J., Lorenz, R. D., Wall, S. D., Kirk, R. L., Wood, C. A., Lunine, J. I., the Cassini Radar Team (2011). Regional geomorphology and history of Titan's Xanadu province. *Icarus*, *211*(1), 672–685. https://doi.org/10.1016/j.icarus.2010.07.022

Radebaugh, J., Ventra, D., Lorenz, R. D., Farr, T., Kirk, R., Hayes, A., et al. (2016). Alluvial and fluvial fans on Saturn's moon Titan reveal processes, materials and regional geology. In D. Ventra & L. E. Clarke (Eds.), *Geology and geomorphology of alluvial and fluvial fans: Terrestrial and planetary perspectives*, *Special Publication* (Vol. 440). London: Geological Society. https://doi.org/10.1144/SP440.6

Rannou, P., Toledo, D., Lavvas, P., D'Aversa, E., Moriconi, M. L., Adriani, A., et al. (2016). Titan's surface spectra at the Huygens landing site and Shangri-La. *Icarus*, *270*, 291–306. https://doi.org/10.1016/j.icarus.2015.09.016

Rodriguez, S., Garcia, A., Lucas, A., Appéré, T., Le Gall, A., Reffet, E., et al. (2014). Global mapping and characterization of Titan's dune fields with Cassini: Correlation between RADAR and VIMS observations. *Icarus*, *230*, 168–179. https://doi.org/10.1016/j.icarus.2013.11.017

Rodriguez, S., Le Mouélic, S., Sotin, C., Clénet, H., Clark, R. N., Buratti, B., et al. (2006). Cassini/VIMS hyperspectral observations of the Huygens landing site on Titan. *Planetary and Space Science*, *54*(15), 1510–1523. https://doi.org/10.1016/j.pss.2006.06.016

Savage, C. J., Radebaugh, J., Christiansen, E. H., & Lorenz, R. D. (2014). Implications of dune pattern analysis for Titan's surface history. *Icarus*, *230*, 180–190. https://doi.org/10.1016/j.icarus.2013.08.009

Schröder, S. E., Karkoschka, E., & Lorenz, R. D. (2012). Bouncing on Titan: Motion of the Huygens probe in the seconds after landing. *Planetary and Space Science*, *73*(1), 327–340. https://doi.org/10.1016/j.pss.2012.08.007

Schröder, S. E., & Keller, H. U. (2008). The reflectance spectrum of Titan's surface at the Huygens landing site determined by the descent imager/spectral radiometer. *Planetary and Space Science*, *56*(5), 753–769. https://doi.org/10.1016/j.pss.2007.10.011

Singh, S., Cornet, T., Chevrier, V. F., Combe, J. P., McCord, T. B., Roe, L. A., et al. (2016). Near-infrared spectra of liquid/solid acetylene under Titan relevant conditions and implications for Cassini/VIMS detections. *Icarus*, *270*, 429–434. https://doi.org/10.1016/j.icarus.2015.11.002

Soderblom, J. M., Brown, R. H., Soderblom, L. A., Barnes, J. W., Jaumann, R., Le Mouélic, S., et al. (2010). Geology of the Selk crater region on Titan from Cassini VIMS observations. *Icarus*, *208*(2), 905–912. https://doi.org/10.1016/j.icarus.2010.03.001

Soderblom, L. A., Kirk, R. L., Lunine, J. I., Anderson, J. A., Baines, K. H., Barnes, J. W., et al. (2007). Correlations between Cassini VIMS spectra and RADAR and SAR images: Implications for Titan's surface composition and the character of the Huygens probe landing site. *Planetary and Space Science*, *55*(13), 2025–2036. https://doi.org/10.1016/j.pss.2007.04.014

Sohl, F., Sears, W. D., & Lorenz, R. D. (1995). Tidal dissipation on Titan. *Icarus*, *115*(2), 278–294. https://doi.org/10.1006/icar.1995.1097

Solomonidou, A., Coustenis, A., Hirtzig, M., Rodriguez, S., Stephan, K., Lopes, R. M. C., et al. (2016). Temporal variations of Titan's surface with Cassini/VIMS. *Icarus*, *270*, 85–99. https://doi.org/10.1016/j.icarus.2015.05.003

Solomonidou, A., Coustenis, A., Lopes, R. M. C., Malaska, M. J., Rodriguez, S., Drossart, P., et al. (2018). The spectral nature of Titan's major geomorphological units: Constraints on surface composition. *Journal of Geophysical Research: Planets*, *123*, 489–507. https://doi.org/10.1002/2017JE005477

Solomonidou, A., Hirtzig, M., Coustenis, A., Bratsolis, E., Le Mouélic, S., Rodriguez, S., et al. (2014). Surface albedo spectral properties of geologically interesting areas on Titan. *Journal of Geophysical Research: Planets*, *119*, 1729–1747. https://doi.org/10.1002/2014JE004634

Sotin, C., Jaumann, R., Buratti, B. J., Brown, R. H., Clark, R. N., Soderblom, L. A., et al. (2005). Release of volatiles from a possible cryovolcano from near-infrared imaging of Titan. *Nature*, *435*(7043), 786–789. https://doi.org/10.1038/nature03596

Stiles, B. W., Hensley, S., Gim, Y., Bates, D. M., Kirk, R. L., Hayes, A., the Cassini Radar Team (2009). Determining Titan surface topography from Cassini SAR data. *Icarus*, *202*(2), 584–598. https://doi.org/10.1016/j.icarus.2009.03.032

Tobie, G., Grasset, O., Lunine, J. I., Mocquet, A., & Sotin, C. (2005). Titan's internal structure inferred from a coupled thermal-orbital model. *Icarus*, *175*(2), 496–502. https://doi.org/10.1016/j.icarus.2004.12.007

Tobie, G., Lunine, J. I., & Sotin, C. (2006). Episodic outgassing as the origin of atmospheric methane on Titan. *Nature*, *440*(7080), 61–64. https://doi.org/10.1038/nature04497

Tomasko, M. G., Archinal, B., Becker, T., Bézard, B., Bushroe, M., Combes, M., et al. (2005). Rain, winds and haze during Huygens probe descent to Titan surface. *Nature*, *438*(7069), 765–778. https://doi.org/10.1038/nature04126

Tomasko, M. G., Doose, L., Engel, S., Dafoe, L. E., West, R., Lemmon, M., et al. (2008). A model of Titan's aerosols based on measurements made inside the atmosphere. *Planetary and Space Science*, *56*(5), 669–707. https://doi.org/10.1016/j.pss.2007.11.019

Villa, A., Chanussot, J., Benediktsson, J. A., & Jutten, C. (2011). Spectral unmixing for the classification of hyperspectral images at a finer spectral resolution. *IEEE Journal of Selected Topics in Signal Processing*, *5*(3), 521–533. https://doi.org/10.1109/JSTSP.2010.2096798

Vinatier, S., Bézard, B., Nixon, C. A., Mamoutkine, A., Carlson, R. C., Jennings, D. E., et al. (2010). Analysis of Cassini/CIRS limb spectra of Titan acquired during the nominal mission I. Hydrocarbons, nitriles and CO_2 vertical mixing ratio profiles. *Icarus*, *205*(2), 559–570. https://doi.org/10.1016/j.icarus.2009.08.013

Willacy, K., Allen, M., & Yung, Y. (2016). A new astrobiological model of the atmosphere of Titan. *Astrophysical Journal*, *829*(2), 79. https://doi.org/10.3847/0004-637X/829/2/79

Williams, D. A., Radebaugh, J., Lopes, R. M., & Stofan, E. R. (2011). Geomorphologic mapping of the Menrva region of Titan using Cassini RADAR data. *Icarus*, *212*(2), 744–750. https://doi.org/10.1016/j.icarus.2011.01.014

Wood, C. A., Lorenz, R. D., Kirk, R. L., Lopes, R. M., Mitchell, K. L., & Stofan, E. R. (2010). Impact craters on Titan. *Icarus*, *206*(1), 334–344. https://doi.org/10.1016/j.icarus.2009.08.021

Zebker, H. A., Gim, Y., Callahan, P., Hensley, S., Lorenz, R., the Cassini Radar Team (2009). Analysis and interpretation of Cassini Titan radar altimeter echoes. *Icarus*, *200*(1), 240–255. https://doi.org/10.1016/j.icarus.2008.10.023